This is a non-peer reviewed preprint that has been submitted for publication in Journal of Structural Geology.

Dissolution precipitation creep as a process for the strain localisation in mafic rocks

Amicia L. Lee[1*], Holger Stünitz[1, 2], Mathieu Soret[2], Matheus A. Battisti[3]

[*]*amicia.lee@uit.no*

[1]*Department of Geosciences, UiT – Arctic University of Norway, Norway*

[2]*Institut des Sciences de la Terre (ISTO), Université d´Orléans, France*

[3]*Instituto de Geociências, Universidade Federal do Rio Grande do Sul, Brazil*

Twitter: @amicialee

Abstract

Unaltered mafic rocks consist of mechanically strong minerals (e.g. pyroxene, plagioclase and garnet) that can be deformed by crystal plastic mechanisms only at high temperatures (>800°C). Yet, many mafic rocks do show extensive deformation by non-brittle mechanisms when they have been subjected to lower temperature conditions. In such cases, the deformation typically is assisted by mineral reactions. Here we show that dissolution-precipitation creep (as a type of diffusion creep) plays a major role in deformation of gabbro lenses at upper amphibolite facies conditions. The Kågen gabbro exposed on south Arnøya is comprised of almost undeformed gabbro lenses with sheared margins wrapping around them. The shearing has taken place at temperatures of 690 ± 25 °C and pressures of 1.0 to 1.1 GPa. This contribution analyses the evolution of the microstructures and fabric of the low strain gabbro to high strain margins. Microstructural and crystallographic preferred orientation (CPO) data indicate that dissolution-precipitation creep is the dominant deformation mechanism, where dissolution of the gabbro took place in reacting phases of clinopyroxene and plagioclase, and precipitation took place in the form of new minerals: new plagioclase and clinopyroxene (with different composition), amphibole, and garnet. Amphibole shows a strong CPO that is primarily controlled by its preferential growth in the stretching direction. Synchronous deformation and mineral reactions of clinopyroxene suggest that mafic rocks can become mechanically weak during a general transformation weakening process, i.e. the interaction of mineral reaction and deformation by diffusion creep. The weakening is directly connected to a fluid-assisted transformation process that facilitates diffusion creep deformation of strong minerals at far lower stresses and temperatures than dislocation creep. Initially strong lithologies can become weak, provided that reactions can proceed during deformation; the transformation process itself is an important weakening mechanism in mafic

(and other) rocks, facilitating deformation at low differential stresses and low stress exponents.

1. Introduction

Strain localisation and fabric development in the lower continental and oceanic crust are controlled by the active deformation mechanisms. The lower continental crust is, on average, mafic in composition and primarily composed of plagioclase and amphibole or pyroxene (Rudnick & Fountain 1995), minerals that have been shown experimentally to remain mechanically strong up to high temperatures (Mauler *et al.* 2000, Bystricky & Mackwell 2001, Rybacki & Dresen 2004, Moghadam *et al.* 2010). The same applies to the lower oceanic crust. Understanding the mechanisms of such deformation advances our ability to quantify the stresses, rates of deformation processes, and to infer general conditions and environment of the tectonic setting of lower crustal rocks.

Viscous deformation in the crust occurs primarily by two mechanisms; dislocation creep and diffusion creep combined with grain boundary sliding (GBS). Dislocation creep involves intracrystalline deformation, where dislocations move through the crystal lattice by processes of glide. Climb is required to minimise the internal strain energy resulting from dislocation glide. The process of diffusion creep is the result of solid-state diffusion of atoms (diffusive mass transfer) through a crystal lattice, termed Nabarro-Herring creep, or along grain boundaries, termed Coble creep (Poirier 1985, Wheeler 1992, Langdon 2006). If diffusion is combined with dissolution in and precipitation from an aqueous fluid, pressure solution allows material to be transported along grain boundaries in a fluid film rather than the movement of atoms and vacancies (Rutter 1983). Coble creep and pressure solution are efficient processes

at lower temperatures than Nabarro-Herring creep and are far more likely to be dominant in crustal materials (Elliott 1973, Poirier 1985). Dissolution-precipitation creep (DPC) is a term generally used for the process of dissolving and precipitating material during diffusion creep. DPC can occur within a single phase or it may be accompanied by metamorphic reactions and the material is precipitated as a new phase, resulting in transformation weakening (e.g. Stünitz *et al.* 2020).

Amphibole and plagioclase are common mid to lower crustal minerals and as a consequence they are considered to play a large role in controlling the strength of crustal scale structures (Rudnick & Fountain 1995, Tatham *et al.* 2008, Lloyd *et al.* 2011). The strength and active deformation mechanisms of plagioclase at mid to lower crustal conditions have been the subject of many studies (e.g. Marshall & McLaren 1977, Tullis 1983, A. Dimanov *et al.* 1999, Kruse *et al.* 2001, H. Stünitz *et al.* 2003, Rybacki & Dresen 2004, Terry & Heidelbach 2006, Miranda *et al.* 2016), yet the rheology of mafic minerals have received very little attention so far (Bystricky & Mackwell 2001, Dimanov *et al.* 2003, 2011, Dimanov & Dresen 2005, Moghadam *et al.* 2010), and that of amphibole remains poorly understood.

Experimentally, amphibole is considered to be strong at lower crustal conditions (Brodie and Rutter, 1985; Shelley, 1994), and only exhibits weakening with mechanical twinning and dislocation glide at high stresses and strain rates (Rooney *et al.* 1970, 1975, Dollinger & Blacic 1975, Morrison-Smith 1976, Hacker & Christie 1990) and exhibits a fabric during diffusion creep and reaction (Getsinger and Hirth 2014). Naturally deformed amphiboles have been shown to display brittle deformation at greenschist to amphibolite facies conditions (Allison & La Tour 1977, Brodie & Rutter 1985, Nyman *et al.* 1992, Stünitz 1993, Babaie & La Tour 1994, Imon *et al.* 2004, Soret *et al.* 2019). Evidence for crystal plasticity has been interpreted (often

based upon CPO) in natural samples at temperatures from 450 to >650°C via dynamic recrystallization, dislocation creep on (100)[001] and subgrain formation by dislocation glide (Biermann & van Roermund 1983, Cumbest *et al.* 1989, Skrotzki 1992, Siegesmund *et al.* 1994, Díaz Aspiroz *et al.* 2007, Pearce *et al.* 2011). Additionally, evidence for diffusion creep of natural amphibole has been inferred by dissolution-precipitation creep and/or diffusion-accommodated GBS and diffusive mass transfer at upper greenschist to lower amphibolite facies conditions have been observed to form strong fabrics (Berger & Stünitz 1996, Imon *et al.* 2002, 2004, Okudaira *et al.* 2015, Soret *et al.* 2019, Mansard *et al.* 2020b). Naturally deformed amphibole usually produces strong fabrics and is thought to be responsible for the strongly anisotropic lower crust (Mainprice & Nicolas 1989, Tatham *et al.* 2008, Lloyd *et al.* 2011, Ji *et al.* 2013).

From the short summary of literature results above, it emerges that the relationships between chemical reactions, fabric formation, and deformation mechanisms in mafic rocks are poorly understood, yet they play a major role for understanding the mechanical strength of the crust and for localizing deformation in different tectonic settings. In this study, we use samples from the deformed margin of the Kågen gabbro (N. Norwegian Caledonides) to show the influence of fluid on active deformation mechanisms and strain localisation during deformation at amphibolite facies conditions.

2. Geological setting

The Caledonides formed from convergence and collision of Baltica and Laurentia during the Silurian to Devonian periods. In northern Norway, large-scale nappe stacking preserves a section of autochthonous Baltica basement and ophiolites with varying metamorphic grades

and deformation style (Corfu *et al.* 2014). The Reisa Nappe Complex (from bottom to top: Vaddas, Kåfjord, and Nordmannvik nappes; Figure 1a) in northern Troms is considered to be Iapetus-derived or part of the outer Baltica margin (Andersen *et al.* 1982, Corfu *et al.* 2006). It underwent viscous deformation and metamorphism at amphibolite- to granulite-facies conditions with pervasive partial melting (Roberts & Sturt 1980, Faber *et al.* 2019).

The Kågen gabbro intruded into amphibolite to granulite-grade metasediments of the Vaddas Nappe and is exposed on the islands of Kågen and Arnøya (Figure 1b). The emplacement of the gabbro occurred at 439±1 Ma (U-Pb zircon concordia age; Faber *et al.* 2019), and cooling is recorded over a broad temperature range of 650-900°C at pressures of 7-9 kbar that correspond to depths of 26-34 km resulting in partial melting of the adjacent felsic and metapelitic rocks (Getsinger *et al.* 2013, Gasser *et al.* 2015, Faber *et al.* 2019). A mantle melt source and extensional setting is implied from the tholeiitic composition of the gabbro in the Vaddas Nappe (Lindahl *et al.* 2005).

The sample location is situated near the western margin of the Kågen gabbro on Arnøya (GR: 70.04389N, 20.71444E). The outcrop region consists of undeformed gabbro lenses with mylonitised margins enveloping the lenses (Figure 2a), and is approximately 0.5 km west of samples studied by Getsinger *et al.* (2013). The area studied by Getsinger *et al.* (2013) hosts several hydrous pegmatite intrusions that locally hydrated the gabbro and partitioned deformation. The deformed margins of gabbro pods in our sample area are not associated with pegmatite intrusions, and, together with the formation of a regional fabric close to margin of the gabbro body, indicate a different setting for the deformation.

The Vaddas Nappe underwent shearing at 432±6 Ma (TIMS, mean $^{206}Pb/^{238}U$ age in titanite), temperatures of 630-640°C, pressures of 12-13 kbar and depths 43-46 km during the main

Scandian collision event of the Caledonides (Faber *et al.* 2019), and the gabbro outcrops have been deformed during this orogenic stage. This paper investigates the processes occurring during deformation of mafic rocks and where the observed deformation in the Kågen gabbro is related to the Vaddas Nappe and Caledonian deformation history.

3. Methods of study

In this paper we analysed polished thin sections in order to investigate the features of strain variation through A8B. The sample is cut in the X-Z section of the kinematic reference frame. Where minerals have been abbreviated, we follow the database from Whitney & Evans (2010).

3.1 Electron microscopy

Electron probe microanalysis was carried out at CAMPARIS (Sorbonne University, Paris, France) using a Cameca SX-Five instrument. Point measurements were made using 15 kV accelerating voltage, a 10 nA beam current with a 1 µm spot size. Composition maps were acquired using a 15 kV accelerating voltage, a 40 nA beam current with a 1 µm spot size and 50 ms dwell time. The instrument was calibrated using diopside (Ca, Mg, Si), MnTiO3 (Mn, Ti), orthoclase (K, Al), Fe2O3 (Fe), albite (Na) and Cr2O3 (Cr) as standards to measure elements in brackets. Selected representative analyses of garnet, clinopyroxene, plagioclase and amphibole from point analysis are shown in Table 1.

3.2 *Thermodynamic modelling and empirical thermo-barometry*

Several empirical thermo-barometers were used to estimate the pressure-temperature conditions of formation of the mineral assemblages observed in the low, mid and high strain zones. The crystallization temperatures of metamorphic garnet and clinopyroxene pairs at microstructural equilibrium were estimated using the thermometer of Powell (1985). For these estimates, pressure was taken to be ~1 GPa - a conservative assumption as garnet–clinopyroxene thermometry is poorly dependent on pressure (pressure variations of 0.5 GPa affect the temperature by ≤ 15°C). The crystallization temperatures of amphibole and plagioclase pairs were calculated using the combined thermo-barometers of Holland & Blundy (1994) and Molina *et al.* (2015).

The pressure-temperature conditions of the high strain layers were also estimated using forward thermodynamic modelling (Perple_X software version 6.8.6; (Connolly & Kerrick 1987, Connolly 2009). The pseudosection was modelled in the NCKFMASH system using the internally consistent thermodynamic dataset (hp11ver.dat) of Holland & Powell, (2011). The following solution models were used: White *et al.* (2014) for orthopyroxene, biotite, chlorite and garnet, Green *et al.* (2016) for mafic melts, augite and hornblende, and Holland & Powell (2003) for plagioclase and K-feldspar. The H_2O value was set to 1.1 wt% after calculating a T-X(H_2O) diagram with a water content ranging from 0.5 to 2 wt% (i.e., excess water) at a pressure of 1 GPa, consistent with the estimates from the amphibole-plagioclase thermo-barometry (Holland & Blundy 1994, Molina *et al.* 2015). The H_2O value is also consistent with the proportion of amphibole (~ 50 vol.%) observed in the high strain layers (see section 4.1.3).

3.3 Electron backscattered diffraction (EBSD)

Crystallographic orientation data was collected via electron backscattered diffraction (EBSD) Oxford Instruments Nordlys S detector also on the Zeiss Merlin SEM at the University of Tromsø. Crystallographic data were collected using 20 kV accelerating voltage, 70° specimen tilt angle and 24-29 mm working distance. Detailed maps were measured with a step size of 1-3 µm and 7 bands detected. Oxford Instruments Aztec software was used for data acquisition and initial data processing, MTEX v.5.2.8 open source software toolbox (Bachmann *et al.* 2010) for MATLAB was used for enhanced data processing and pole figure plotting. Individual crystal orientations with median absolute deviation (MAD) values >1.0 were removed. Individual grains were reconstructed using the 'calcGrains' function in MTEX using a 10° misorientation cut-off relative to neighbouring solutions. Pole Figures were created for the mean orientation of each grain based on the orientation distribution function (ODF), using the 'calcDensity' function. The mean orientation of each individual grain was then plotted on lower hemisphere, equal area pole figures such that each data point represents a single grain on the pole figure, which are subsequently contoured.

Grain size and shape parameters are calculated using grains calculated from the EBSD map data. The grain size is calculated via the equivalent radius and multiplied by 2 giving the size. Grain orientation is calculated using a fitted ellipse and orientation of the long axis. The grain data for low (1a, 1b, 2a, 2b, 3a, 10a, 10b), mid (3c, 4b, 4c, 5a, 5b, 6a) and high (3b, 3d, 4a, 7a, 7b, 8a, 9a, 9b) strain areas have been grouped together to give an overview of grain shape parameters in each of the strain zones.

4. Results

4.1 Sample description

The outcrop displays strain gradients from weakly deformed low strain domains to high strain mylonites (Figure 2). Concurrent with the deformation, mineral reactions transform the original mineral assemblage of the gabbro. The fact that the mineral reactions take place simultaneously with the deformation is documented by the microstructures, which indicate synkinematic reactions (Figure 3, 4). As will be described below, the mineral assemblages and their compositions indicate a progressive adjustment to changing pressure and temperature conditions. Thus, the deformation and reactions took place progressively over a certain period of time, during which the ambient physical conditions were changing. The acquisition of increasing shear strain occurred in sequential steps, which are interpreted to preserve the different stages of shear zone development during which deformation had progressively localized as the material weakened (type 2 shear zones of Means 1995). Such a development allows the interpretation that low strain domains preserve earlier stages of the deformation history and high strain domains the latest stages.

The sample is comprised of transitional fabrics from low to high strain. The original undeformed gabbroic fabric is never preserved in low strain domains (Figure 2). The plagioclase is often more deformed than the pyroxene domains and forms a weak foliation. Semi-quantitatively, foliation formation is used as an expression of strain intensity, increasing outward from the inner low strain domains towards the high strain margins (Figure 2). Mid-strain domains allow a clear distinction of domains of mafic and plagioclase-derived minerals, and this distinction develops into thin layers in most high strain zones (Figure 2c). In some cases, there is no distinct separation of phases into layers but, instead, a more homogeneous distribution. Below, we present the results for microstructural and chemical properties and crystallographic preferred orientation (CPO) of each type of domain (low, mid and high strain zones).

218

219 *4.1.1 Low strain zones*

220 The primary phases in the low strain zones are clinopyroxene and plagioclase with minor
221 orthopyroxene, amphibole ilmenite and zoisite (Figure 3a-b). The original igneous gabbro
222 assemblage has been metamorphosed; pyroxenes are rimmed by amphibole, and zoisite
223 needles with more albitic plagioclase replace original plagioclase grains. There are two
224 populations of clinopyroxene grains; large grains that are 3-6 mm in size with undulose
225 extinction, and smaller grains (up to 200 μm in size) that mantle some of the large
226 clinopyroxene grains (Figure 3a-b, 4a-b). The large grains commonly have exsolution lamellae
227 of amphibole and ilmenite. Some large clinopyroxene grains have recrystallized portions that
228 follow cleavage cracks in the original grain; these are composed of both clinopyroxene and
229 amphibole (Figure 4a-b). The amphibole rims enclose clinopyroxene grains but have a larger
230 grain size in the clinopyroxene pressure shadows, 50 vs. 100 μm (Figure 4a-f, 5a). Shape and
231 size analysis of amphibole grains show a unimodal grain size distribution with a mean grain
232 size of 68 μm and grains elongated parallel to the foliation (Figure 5a, d). There are two
233 populations of plagioclase; the first comprises of large grains up to 3 mm with undulose
234 extinction, deformation twins and zoisite needles (Figure 4c). The second population is
235 recrystallized 50-300 μm plagioclase with twins, straight extinction and ~120° triple junctions.

236 The orthopyroxene grains have mostly been replaced by amphibole; the few relicts that
237 remain are recrystallized. Ilmenite is found adjacent to clinopyroxene grains and often exhibits
238 amphibole coronas. Olivine is not found in the A8B sample, but it is present in undeformed
239 gabbro c.700 m east as detailed by Getsinger *et al.* (2013). The orthopyroxene typically is a
240 reaction product of an olivine + plagioclase reaction that took place before the deformation.

241

242 *4.1.2 Mid strain zones*

243 Towards the margins of the gabbro pods, the foliation is progressively better developed
244 (Figure 3c-d). Clinopyroxene, plagioclase and amphibole are the dominant phases with trace
245 amounts of garnet, zoisite, quartz and ilmenite whilst orthopyroxene is not present.
246 Clinopyroxene relict grains are 0.5-2 mm, smaller than in the low strain areas of the rock. The
247 primary clinopyroxene grains have undulose extinction and the amphibole exsolution lamellae
248 can occur as 'blebs'. The recrystallized tails have a granoblastic texture without signs of
249 internal grain deformation (Figure 4d-e). The amphibole rims are coarser, up to 200 µm, and
250 surround recrystallized tails of the clinopyroxene. Quartz is present in trace volumes between
251 some clinopyroxene grains and the amphibole rims. There are zones where amphibole has
252 almost completely replaced the clinopyroxene (e.g. top of Figure 4f), in these zones the
253 amphibole grain size is up to 500 µm. Within these bands, there are minor amounts of
254 clinopyroxene, quartz and ilmenite. Despite this observed grain size increase, the average
255 grain size is only 64 µm as there is a high proportion of small amphibole grains associated with
256 the clinopyroxene replacement (Figure 4d-f, 5b). Similarly to the clinopyroxene, the large
257 plagioclase grains are smaller in the mid strain zone (up to 2 mm), but still exhibit undulose
258 extinction and deformation bands. The recrystallized plagioclase grains show little internal
259 deformation but some grain boundaries are more lobate than in the low strain zones (Figure
260 4e). The amphibole and plagioclase grains in the mid strain areas are orientated with their
261 long axis parallel to the foliation (Figure 5e). Prismatic zoisite is up to 500 µm in length within
262 large plagioclase grains where they are loosely aligned to the foliation but zoisite is also
263 present in the smaller plagioclase grains with a random orientation (Figure 4c, e). In some mid

264 strain areas garnet grows in bands, the grains are up to 100 µm in size, are faceted with low-
265 index planes, and have equant shape with quartz inclusions (Figure 4d-e).

266

267 *4.1.3 High strain zones*

268 At the edges of the gabbro pods, the rock is strongly deformed and appears mylonitic in the
269 field (Figure 2c). The foliation is well developed in the high strain zones exhibiting alternating
270 bands of amphibole and plagioclase with garnet bands (Figure 3e-f). The amphibole bands
271 have trace amounts of clinopyroxene, quartz, calcite, and ilmenite interspersed (Figure 4g-i).
272 The amphibole grains are up to 600 µm in length and a mean grain size of 91 µm (Figure 5c).
273 Amphibole shows the strongest SPO of the different strained zones with grains strongly
274 orientated parallel to the shear direction, and also to the foliation (Figure 5f). The plagioclase
275 bands are recrystallized and no longer contain any of relicts of original grains (porphyroclasts;
276 Figure 4g-i). Plagioclase is also present in mixed bands with amphibole, forming polyphase
277 layers (Figure 4i). In such layers, the mean grain size has decreased to 83 µm and the grain size
278 distribution is virtually identical to amphibole (Figure 5c). The plagioclase grains show a similar
279 long axis orientation in the mid and high strain areas (Figure 5 e-f). Quartz is present as
280 interstitial blebs and inclusions within amphibole and plagioclase. Calcite and ilmenite are
281 both cuspate in shape, infilling pore space in the rock. Zoisite is rarely present in high strain
282 zones, when found it is less than 20 µm and randomly orientated (Figure 4h). Garnet bands
283 up to 4 mm in width are commonly associated with amphibole-feldspar band alternation
284 (Figure 4g). Isolated garnet grains are also present within amphibole layers. The garnets are
285 subhedral, typically 1-3 mm in size and are associated with quartz and calcite. Quartz is

present as inclusions and interstitial blebs whilst calcite infills the pore space around garnets (Figure 4g-h).

4.2 Mineral chemistry

Clinopyroxene has a diopside-rich composition with a Mg# [Mg/(Mg+Fe)] ranging between 0.65 and 0.80 (Figure 6a, Table 1). Magmatic porphyroclasts (samples A8B1, A8B4) show higher values (0.75-0.80) than new small grains at their rims and tails (0.75-0.72). New metamorphic grains scattered in the matrix (sample A8B4) show the lowest Mg# values (0.65-0.73). The amount of Na, representing the jadeite content, varies between 0.3 and 0.5 a.p.f.u. regardless of the microstructural position. The changes in Mg and Na content are illustrated in Figure 7a-b, new small grains surrounding or forming tails around magmatic porphyroclasts have lower MgO and higher Na_2O value than the original clinopyroxene grain. All analyses are available as supplementary material.

Amphibole analyses plot within the pargasite to actinolite fields (nomenclature from Leake *et al.* 1997; Figure 6b). The Mg# varies between 0.50 and 0.75, and the Ti ranges up to 0.25 a.p.f.u (Figure 6c, Table 1). The Mg# shows a continuous increase, and the Ti a continuous decrease versus increasing Si, with clear microstructural relations (Figure 7). Amphibole crystallizing after the magmatic clinopyroxene porphyroclasts in the low and mid strain zones (samples A8B1, A8B4) has the highest Mg# (> 0.60) and Si values (> 6.6 a.p.f.u.) and the lowest Ti content (< 0.1 a.p.f.u.). In the low, mid and high strain zones, amphibole co-existing with secondary plagioclase has lower Mg# (<0.63) and Si values (<6.6 a.p.f.u) with generally higher Ti content (0.06-0.16 a.p.f.u.). While amphibole included in garnet in the mid strain zone has the same

composition as amphibole in the plagioclase-rich layers, amphibole included in garnet the high strain zone shows the highest Ti content (0.12-0.24).

Feldspar is plagioclase with an anorthite content [Ca/(Ca+Na)] varying between 0.25 and 0.60 Figure 6d). A correlation is observed with both the microstructural position and the fabric intensity. In the low (A8B1) and mid (A8b4) strain zone, the cores of magmatic porphyroclasts (Figure 7a) have the highest anorthite content (0.54-0.60). The prophyroclast rims and new small grains at microstructural equilibrium with amphibole in such samples (Figure 7a, c) show an intermediate composition (values of 0.35-0.55). A similar distribution is observed for the new recrystallized plagioclase grains equilibrated with amphibole in the high strain zone, varying from 0.28 to 0.45. Plagioclase in the garnet-amphibole bearing layers from the mid and high strain zones (samples A8B4, A8B9) have the lowest anorthite content (0.25-0.40).

The garnet chemical composition in the amphibole-free layers of the mid strain zones varies in function of the neighbouring minerals (Figure 6e-f). Crystal faces next to clinopyroxene are enriched in Fe and Mg (Alm: 0.59, Prp: 0.15, Grs: 0.23, Sps: 0.02) while faces next to plagioclase are enriched in Ca (Alm: 0.51, Prp: 0.10, Grs: 0.36, Sps: 0.02). Mn content remains constant and seems not be affected by the neighbouring minerals. Garnet in the amphibole-rich layers of the high-strain zones shows a more homogeneous composition (Alm: 0.53-0.57, Prp: 0.13-0.14, Grs: 0.25-0.29, Sps: 0.05) that lies in-between the two garnet compositions recognized in the mid-strain zones.

Mineral chemistry exhibits local microstructural variations within the gabbro. For example, Figures 6a and 7a-b show the change in Mg-content between clinopyroxene porphyroclasts and adjacent new grains. The garnet grain B in Figure 6e shows how garnet chemistry varies when adjacent to clinopyroxene or plagioclase. The garnet rim round a clinopyroxene grain

shows a variation in Mg content (Figure 7c); when adjacent to plagioclase it is more depleted than the core which is adjacent to clinopyroxene and ilmenite. Figure 7d shows a chemical map in a high strain amphibole area and how the chemistry varies between the olive green (top) and jade green (bottom) coloured amphibole (Fig. 4h-i); the olive green coloured amphibole has higher Mg and Si values compared to the jade green coloured amphibole. In addition the olive green coloured amphibole exhibits zoning, with a decreasing of Mg and Si content from core to rim.

4.3 Pressure-temperature estimates

The amphibole-plagioclase thermo-barometry (Holland & Blundy 1994, Molina *et al.* 2015) yielded results for three samples of the low, mid and high strain zones (samples A8B1, A8B4 and A8B9, respectively). They all show similar P-T conditions of 690 ± 25°C and 10.5 ± 1.5 kbar (Figure 8 inset). Crystallization temperatures in the mid strain zone were also calculated using the garnet-clinopyroxene thermometer of Powell (1985). Metamorphic pairs at textural equilibrium yielded 700 ± 25°C at 10 kbar (Figure 8 inset).

Peak P-T conditions of the high strain zone were additionally constrained using thermodynamic modelling. The best fit of the garnet, amphibole and plagioclase isopleths lies in the field with Amph + Cpx + Grt + Pl + Qz (without free-water), around 675 ± 25°C and 10.5 ± 0.5 kbar (Figure 8). The predicted mineral compositions (isopleths) match those documented by mineral analyses in this study. The modelled temperatures and pressures are in very good agreement with those of the thermo-barometry.

4.4 Crystallographic preferred orientation (CPO)

Crystallographic preferred orientations (CPO) of amphibole and clinopyroxene were measured at 1-3 µm step size in maps of ~16 mm^2. Figure 9 shows lineation-parallel (= X-pole-figure-axis) amphibole orientation maps, CPO pole figures, and inverse pole figures (IPF) of amphibole and clinopyroxene. Clinopyroxene CPO's are only shown for low and mid strain areas as there are insufficient grains in the high strain areas to construct statistically meaningful pole figures. All individual phase maps and CPO pole Figures for amphibole, clinopyroxene and plagioclase are available in supplementary information (Figure S1-4).

In the low strain areas, amphibole CPO is characterised with the (100) plane subnormal to the shear plane (XY-pole figure-section; Figure 9, bottom), and the [001] axes subparallel to the shear direction (X-axis). The amphibole J index is 8.26 and the M index is 0.305 for the example low strain zone (A8B1). When the clinopyroxene CPO is considered alongside the amphibole CPO, the maxima are weaker but they are orientated in similar directions. In the mid strain area the amphibole CPO has a similar fabric to the low strain area; the (100) plane is subnormal to the shear plane, and the [001] direction is subparallel to the shear direction. The [001] direction shows a weaker maximum but is aligned closer to the shear direction than the fabric in the low strain areas. For the mid strain zone, the amphibole J index is 3.33 and the M index is 0.201 (A8B4). The clinopyroxene CPO in the mid strain areas is very weak and does not correlate to the amphibole CPO. In the high strain region (A8B9), the amphibole CPO exhibits a girdle and a weak maximum of the (100) plane orientated normal to the shear plane, (010) planes in a weak maximum subnormal to (100) and the shear direction and the [001] direction shows a strong maximum parallel to the shear direction. The amphibole J index is 4.23 and the M index is 0.157 for the high strain area.

The relationship between the amphibole and clinopyroxene CPO is further explored in Figure 10 where four regions of a clinopyroxene grain with amphibole replacement has been studied. Region A shows the CPO for the clinopyroxene grain and all surrounding amphibole grains. This amphibole CPO fabric is weak and the maxima are directly related to maxima in the clinopyroxene CPO. Region B focusses on the left hand side of the main clinopyroxene grain, which has undergone more recrystallization than the right. The CPO fabric is almost identical to region A, but is much stronger (for clinopyroxene and amphibole) than in region B. Region C shows the fabric for the right hand side of the clinopyroxene grain and the amphibole inclusions within the grain. The fabric for this area is very strong, the amphibole and clinopyroxene maxima are very similar and are related to the fabrics observed in regions A and B. The final area, region D, considers the tail of the clinopyroxene where the highest amount of recrystallization has occurred. The clinopyroxene CPO for region D is very weak and does not bare a strong resemblance to the amphibole fabric. The amphibole fabric in region D is similar to the whole map amphibole CPO (region A) in the mid strain area in Figure 9b.

The plagioclase CPO is generally weak; in low strain regions there tends to be a very weak CPO (Figure 11a) but the fabric is not consistent between different low strain maps (see Figure S4). The high strain area was analysed in subsets to see if there is a change in CPO strength between monophase and polyphase regions (Figure 11c; e.g. Mehl & Hirth 2008). The CPO is weak and shows no fabric in any of the subsets, for plagioclase. Nevertheless, the amphibole for this (and all other) high strain areas shows a strong CPO with (001) normal to the shear direction and [001] parallel. The quartz, calcite and ilmenite all show disordered CPO fabrics. The plagioclase CPO is also weak in the mid strain zone.

5. Discussion

The Kågen gabbro is a 45 km^2 intrusion with a relatively unaltered and undeformed core. Deformation increases towards its margins with the Vaddas Nappe. The southern coastline of Arnøya provides a transect through the gabbro. The centre of the gabbro is relatively undeformed with a clinopyroxene, olivine, and plagioclase assemblage (Getsinger *et al.* 2013). There is localised deformation in the core of the gabbro where it is cross-cut by fluid-rich pegmatites (Getsinger *et al.* 2013). The deformation in the immediate vicinity to pegmatites is related to fluid released during pegmatite emplacement (late magmatic stage of the gabbro intrusion).

Towards the edges of the gabbro (best exposed in the west), the lenses of weakly deformed gabbro surrounded by high strain margins represent a small scale version of the general strain distribution of the whole gabbro body. The deformation at the gabbro margins overprints the mainly undeformed gabbro body. This suggests the centre of the gabbro did not deform during the subsequent deformation phase, it remained strong and rigid, whilst heterogeneities produced by local mineral reactions at the margins were exploited to localise deformation during nappe emplacement.

5.1 Mineral reactions and P-T-time of deformation

Getsinger *et al.* (2013) studied intrusion related deformation within the centre of the Kågen Gabbro, and observed a similar assemblage to the low strain areas in this study. The undeformed gabbro of Getsinger *et al.* (2013) has higher volumes of olivine and clinopyroxene, and the amphibole rims are absent or not well developed. Clinopyroxene is abundant and the main mafic phase of the gabbro. According to Getsinger *et al.* (2013)

orthopyroxene in the undeformed gabbro is commonly associated with the olivine and has formed as reaction rims around it. Therefore, it is suggested that the initial alteration of the gabbro occurred via olivine reacting with plagioclase forming pyroxene (plus some spinel) rims:

$$Pl + Ol \rightarrow Cpx + Opx \pm Spl. \quad \text{(R1)}$$

Metamorphism of the margins of the Kågen gabbro likely occurred during emplacement and deformation of the Vaddas nappe. This main deformation event resulted in a pyroxene consuming and amphibole producing hydration reaction during nappe emplacement under changed pressure and temperature conditions:

$$Cpx + Opx + Pl(Ca) + H_2O \rightarrow Amp + Pl(Na) + Grt \pm Qz \pm Fe\text{-}Ti\ Ox \pm Zo \pm Cal. \quad \text{(R2)}$$

The least deformed parts of the Kågen gabbro exhibit some preserved assemblages (left hand side of Reaction 1) and some reacted products (right hand side of reaction 1). The high strain regions at the margins represent the final assemblage in Reaction 2 (right hand side of reaction 2). The low and mid strain areas show the progression of the mineral reaction 2 which is synchronous with deformation. There are remnants of clinopyroxene within some high strain amphibole layers; they represent former clinopyroxene grains that were not fully consumed in the amphibole producing reaction.

Thermodynamic modelling combined with conventional thermo-barometry show that reaction 2 took place at 690 ± 25 °C and 10.5 ± 1.5 kbar (within the uncertainties of the method), which is similar to previously established P-T conditions for the solid state cooling of the gabbro (650-900°C, 7-9 kbar; Getsinger *et al.* 2013). Such a result indicates that the progression of mineral reactions were directly dependent of change in water content in the

bulk rock during deformation. The fluid source is somewhat unknown but intrusion of the gabbro resulted in local migmatization of the surrounding Vaddas metasediments (Faber *et al.* 2019). Solidification of the melt may have released fluids and allowed penetration into the gabbro resulting in localised high strain deformation. On the other hand, the final collision has occurred at ~430 Ma, i.e., ~10 Ma after the emplacement of the gabbro. It may well be that other fluid sources have facilitated the later hydration of the gabbro during deformation.

Generally, in mid strain areas, the clinopyroxene is elongated and partially overgrown/replaced by elongated amphibole rims (Figure 4f). However, in some areas the amphibole rims are absent and the clinopyroxene is mantled by garnet and sometimes ilmenite (Figure 4d-e). Figure 4d shows a clinopyroxene mantled by garnet and ilmenite, yet the clinopyroxene grain above has an amphibole rim. The clinopyroxene grain in Figure 4e has an amphibole rim along the bottom but garnet on top. The absence of amphibole, a hydrated mineral, in these regions suggests a lack of aqueous fluid. These observed microstructural differences demonstrate that fluid availability in the gabbro is extremely localised, and therefore reaction 2 is incomplete in the fluid-deficient parts. In those parts where reaction 2 is complete, as the case of the high strain zones, aqueous fluids must have been more abundant, and therefore we suggest the high strain zones had formed fluid pathways.

The change in chemistry of new vs. magmatic clinopyroxene grains and the change in amphibole chemistry when it neighbours different minerals (e.g. clinopyroxene, plagioclase or garnet), demonstrates that metamorphic reactions accompanied deformation (Figure 6, 7). New clinopyroxene grains have a different chemical composition from that of the porphyroclasts, indicating homogeneous nucleation. Nucleation of new clinopyroxene with a different chemistry is a response to the change in P-T conditions since gabbro emplacement.

The clinopyroxene becomes unstable as aqueous fluid infiltrates the gabbro and enhances reaction 2 and as a consequence strain localisation. The zoning of amphibole grains shows that it grew during a synkinematic reaction (Figure 7d). The change in mineral chemistry within or between neighbouring grains demonstrates that there has been local equilibrium between phases, most likely due to changes in fluid content. Mineral chemistry variations that are associated with microstructural deformation features indicate that the dominant driving potential for crystallization of clinopyroxene and amphibole has been (local) chemical equilibrium and not internal strain energy, i.e., dynamic recrystallization was not the dominant process for reconstituting the microstructures (Stünitz 1998).

When the P-T conditions for the Kågen gabbro margins are considered alongside the more preserved inner parts of the gabbro (Getsinger *et al.* 2013) in relationship to the surrounding Vaddas Nappe metasediments (Faber *et al.* 2019), the results from this study lie on a P-T path connecting them (Figure 12). This suggests the margins of the Kågen gabbro may record the conditions for early stages of Vaddas Nappe thrusting after the gabbro emplacement, which took place at 439±1 Ma (Faber et al. 2019). The deformation observed in this study is part of the same event as the deformation of the metasediments at the Vaddas-Kalak boundary (432±6 Ma, $^{206}Pb/^{238}U$ ages; Faber et al. 2019), and the timing of the deformation of the gabbro margins can be constrained as between ca. 440-425 Ma.

5.2 Formation of crystallographic preferred orientation (CPO)

During deformation and metamorphism of the Kågen gabbro, the clinopyroxene CPO weakened as clinopyroxene has dissolved, whilst the amphibole fabric strengthened as it precipitated (Figure 9-10). Amphibole nucleation within clinopyroxene grains in the low and

mid strain areas indicate that initially amphibole replaced clinopyroxene topotactically, probably along cleavage cracks, and inherited its crystal orientation from clinopyroxene (Figure 10, region C; e.g. Shannon & Rossi 1964, Handy & Stünitz 2002, McNamara *et al.* 2012). Thus, regions B and C in Figure 10 show strong CPO maxima for amphibole that do not relate to the shear geometry but are instead orientated closely to that the host clinopyroxene grain. In contrast, if we consider regions A and D that include the amphibole rim surrounding fewer clinopyroxene relict grain(s), the (100) plane of amphibole becomes orientated subnormal to the shear direction, and the amphibole [001] axes orientated subparallel to the shear direction. These orientations do not correlate with the weaker clinopyroxene CPO's, particularly in region D (Figure 10), where the clinopyroxene CPO is very weak and does not show a distinct pattern. The morphology of the clinopyroxene grains in the recrystallized tail in region D is similar to that of dynamic recrystallization during crystal plastic deformation, but chemical analysis shows that these new clinopyroxene grains are compositionally different to the original grains (Figure 6a) and must have formed by homogeneous nucleation due to a chemical driving potential. Therefore, we suggest the new grains have primarily formed during the chemical reaction when clinopyroxene adjusts its composition. The reaction takes place during deformation that is accommodated by dissolution-precipitation creep processes that progressively destroy the clinopyroxene CPO and account for the change in chemistry.

Thus, during the subsequent deformation process where amphibole rims and tails are well developed in the mid strain areas, amphibole started to nucleate on the clinopyroxene outer boundaries with the same initial inherited clinopyroxene crystal orientation, but during consumption of the clinopyroxene by reaction, the precipitating amphibole developed a distinct fabric different from the clinopyroxene host-controlled one. The CPO of the amphibole

511 is best interpreted as a growth-controlled fabric, in which the fastest growth direction in
512 amphibole is the [001] axis aligned with the stretching direction.

513 The amphibole fabric in low and mid strain areas is the result of both inheritance and
514 orientated growth parallel to the shear direction as shown by the SPO strength increasing from
515 low to high strain areas (Figure 5 d-f). For the CPO, the (100) plane of clinopyroxene is
516 orientated subnormal to the shear direction, and the [001] axes are orientated subparallel to
517 the shear direction (Figure 9). The initial topotactic replacement of clinopyroxene by
518 amphibole results in a direct inheritance of the clinopyroxene CPO (Figure 10) and a smaller
519 mean grain size in low strain areas (Figure 5a).

520 Amphibole overgrows and precipitates rims and tails around clinopyroxene porphyroclasts
521 (Figure 4a-f, 7). The CPO for these tails is progressively less related and therefore less inherited
522 from the clinopyroxene (Figure 10). The SPO strength for amphibole increases from low to
523 high strain areas suggesting amphibole growth in the high strain areas is orientation controlled
524 (Figure 5e). In the high strain areas, the amphibole CPO exhibits a girdle in the (100) plane
525 subnormal to the shear direction and a strong maxima in the [001] axes parallel to the shear
526 direction. The presence of the girdle in (100) suggests a component of rigid body rotation
527 parallel to [001] (Figure 9). The average amphibole grain size increases by 20 µm from the low
528 to high strain areas and the SPO is very strongly orientated parallel to the shear direction
529 (Figure 5).

530 It is common to observe naturally deformed amphibole with the (100) plane aligned
531 subnormal to the shear plane and the [001] direction aligned subparallel to the shear direction
532 (e.g. Berger & Stünitz 1996, Imon *et al.* 2004, Díaz Aspiroz *et al.* 2007, Tatham *et al.* 2008,
533 Getsinger *et al.* 2013, Okudaira *et al.* 2015, Elyaszadeh *et al.* 2018, Soret *et al.* 2019). This

fabric has been shown to occur under middle to upper amphibolite facies conditions (650-750°C, 6-10 kbar), and commonly shows that amphibole grains are reoriented or grow (sub)parallel to the shear direction (Ko & Jung 2015). The primary slip vector in amphibole is <001>, and a strong amphibole CPO with (100) plane subnormal to foliation and [001] axes parallel to lineation could suggest that (100)<001> easy slip system can be important in generating this type of CPO (Díaz Aspiroz *et al.* 2007). However, in the case of the Kågen gabbro there are amphibole porphyroclasts, from which the amphibole is recrystallized, so that dynamic recrystallization and thus a dislocation creep origin of the amphibole CPO can be excluded. The amphibole CPO observed in the Kågen gabbro is similar to other natural examples, and as amphibole is only present in minor proportions (if at all) in the original gabbro, and we propose that the strong fabric forms during precipitation (homogeneous nucleation) of the amphibole. The girdle of (100) planes in the high strain domains indicates rigid body rotation parallel to [001], and it has been suggested that such girdles are formed through cataclastic flow forming a fine-grained matrix produced by fracturing and comminution (Imon *et al.* 2004, Kanagawa *et al.* 2008, Kim & Jung 2019). Cataclastic flow is unlikely in these samples, because (a) the confining pressures of ~1GPa make frictional processes unlikely, and (b) the larger and uniform grain size in higher strain domains without evidence for fracturing (Figure 3e-f, 4c) do not indicate brittle processes. Instead, the rigid body rotation of amphibole grains in the Kågen gabbro is likely to have occurred via progressive rotation in a mechanically weaker matrix, facilitated by solution transfer, precipitation and grain growth of the amphiboles as these increase in modal amount.

Plagioclase shows a decrease in the mean grain size from low to high strain areas (Figure 5a-c). The larger grain size in low strain areas is due to the preservation of original magmatic

557 plagioclase. As deformation of the gabbro progresses, the large original grains are
558 recrystallized and their composition becomes more sodic (Figure 6d). The recrystallization also
559 results in a slight elongation of plagioclase parallel to the shear direction (Figure 5f). The
560 plagioclase CPO is weak, especially in areas where fine plagioclase coexists with amphibole
561 (Figure 11; Kruse & Stünitz, 1999; Lapworth *et al.,* 2002; Mehl & Hirth, 2008). The low strain
562 areas with a slight CPO fabric is controlled by large original grains and does not represent a
563 characteristic fabric type of crystal plasticity (Figure 11a). The lack of plagioclase CPO in the
564 high strain areas shows a lack of crystal plasticity and the dominant deformation mechanism
565 is inferred to be dissolution-precipitation creep (Figure 11c). The strong amphibole CPO shows
566 that deformation in the Kågen gabbro was controlled by orientated growth rather than a
567 crystal plastic mechanism such as dislocation creep. Figure 11c shows that the plagioclase
568 grain size is smaller in the polyphase areas than the monophase band, suggesting that grain
569 growth is limited in the phases mixed areas. Deformation by diffusion creep in the high strain
570 areas is most likely accommodated by grain boundary sliding that is localised in polyphase
571 layers where phase mixing occurs between amphibole and plagioclase.

572 Quartz, calcite and ilmenite occur interstitially or infill pore space. When the microstructural
573 morphology is considered alongside the lack of CPO fabric, we suggest that these minerals did
574 not undergo any crystal plasticity and precipitated late in the deformation history with no
575 orientation controlled growth.

576

577 5.3 *Wider implications*

578 Deformation of the Kågen gabbro margins was associated with emplacement of the Vaddas
579 Nappe on a P-T path from 690°C and 10.5 kbar to 630°C and 13 kbar (Figure 12a). Crystal

plastic deformation may be expected in plagioclase and clinopyroxene at such conditions (Mauler *et al.* 2000, Rybacki & Dresen 2004), however no evidence for dislocation creep processes is observed here. Instead, we observe a change in chemistry and stable phase assemblage between the low and high strain regions (Figure 12b). Fluid pathways within the gabbro allowed metamorphic reactions to proceed and consequently enhanced strain localisation. The fluid supply was limited or infiltration was not pervasive to allow preservation of the dry, low strain gabbro pods. During emplacement and deformation of the Vaddas Nappe, the high strain zones formed fluid pathways and a network of anastomosing shear zones that localised deformation and left the low strain areas as dry pods (Figure 2).

It is often assumed that new small grains in a deformed rock is the result of dynamic recrystallization, however we show that the new clinopyroxene and plagioclase grains have a different chemistry to the larger original grains (Figure 6, 7). This indicates dissolution-precipitation is responsible for the formation of the new grains rather than a crystal-plastic mechanism. In addition, dislocation creep is considered a fabric strengthening mechanism (e.g. strong CPO) whereas diffusion creep is fabric weakening (e.g. no CPO), but when dissolution-precipitation creep is accompanied by orientated growth, the resultant amphibole CPO is strong. Deformation experiments of plagioclase and pyroxene mixtures by Marti *et al.* (2017, 2018) and Mansard *et al.* (2020a, 2020b) showed that amphibole coronas on pyroxene were more elongated in the deformed samples. These results indicate that amphibole has accommodated displacement via dissolution-precipitation creep. As dissolution precipitation creep is a type of diffusion creep, stress exponents for this type of deformation are expected to be as low as those for diffusion creep, i.e. in the order of $n \sim 1$.

602 The processes that control deformation in the Kågen gabbro (e.g. DPC, rigid body rotation and
603 GBS) are similar to those described in the metamorphic sole of a subduction zone (Soret *et al.*
604 2019). Dissolution-precipitation creep alongside amphibole-forming metamorphic reactions
605 in the Kågen gabbro are driven by variations in water activity. Fluid pathways in the gabbro
606 resulted in strain localisation that in turn controlled the rheology (e.g. Marti *et al.* 2017, 2018,
607 Soret *et al.* 2019, Mansard *et al.* 2020a, 2020b). Thus the deformation processes observed in
608 the Kågen gabbro represent common processes controlling the development of hydrated
609 mafic rocks, regardless of the geological setting.

610

611 **6. Conclusions**

612 Deformation at the margins of the Kågen gabbro on a P-T path from 690°C and 10.5 kbar to
613 630°C and 13 kbar provides a natural example of how dissolution precipitation creep facilitates
614 the deformation of mafic rocks during concomitant mineral reactions. The mechanical
615 properties of mafic rocks during deformation coupled with reactions are substantially weaker
616 than for an assemblage of pyroxene/amphibole and plagioclase without reactions. Through
617 chemical and microstructural analysis we have shown that metamorphic reactions primarily
618 occurred in a fluid-rich environment, which resulted in strain localisation into the hydrating
619 parts of the rock and subsequent weakening as metamorphic reaction progressed. Despite the
620 strong crystal fabric and CPO in amphibole grains, dislocation creep was not the dominant
621 deformation mechanism, instead dissolution-precipitation creep involving diffusion-
622 accommodated GBS and diffusive mass transfer have facilitated the deformation. The CPO is
623 produced by the fastest growth direction and rigid body rotation, i.e. by shape-factors of the
624 precipitating amphibole. When deformation and mineral reactions occur simultaneously,

625 strong rocks can become mechanically weak, at least transiently. Processes like dissolution-
626 precipitation creep allow the mafic rocks to deform viscously at lower temperatures and lower
627 stresses than expected for dislocation creep of the original constituent phases (pyroxene,
628 amphibole, plagioclase).

629

630 **Acknowledgements**

631 The authors thank Amanda Getsinger for sample collection, documentation, and sample
632 cutting. We thank Jiří Konopásek for discussions and suggestions during early chemical
633 analysis. MB thanks CAPES-Diku Project number 88881.117872/2016-01.

634

635 **Data Availability**

636 EBSD data for maps A8B 2b, 4b, 8a and 9b are available to download as channel text files from
637 https://doi.org/10.17632/xhd6gs3fyc.1.

638

639 **7. References**

640 Allison, I. & La Tour, T.E. (1977) Brittle Deforamtion of Hornblende in a Mylonite: a Direct
641 Geometrical Analogoue of Ductile Deformation By Translation Gliding. *Can J Earth Sci*,
642 **14**, 1953–1961. doi:10.1139/e77-166

643 Andersen, T.B., Austrheim, H., Sturt, B.A., Pedersen, S. & Kjaersrud, K. (1982) Rb-Sr whole
644 rock ages from Mageroy, north Norwegian Caledonides. *Nor. Geol. Tidsskr.*, **62**, 79–85.

645 Babaie, H.A. & La Tour, T.E. (1994) Semibrittle and cataclastic deformation of hornblende-

646 quartz rocks in a ductile shear zone. *Tectonophysics*, **229**, 19–30. doi:10.1016/0040-
647 1951(94)90003-5

648 Bachmann, F., Hielscher, R. & Schaeben, H. (2010) Texture analysis with MTEX- Free and
649 open source software toolbox. *Solid State Phenom.*, **160**, 63–68.
650 doi:10.4028/www.scientific.net/SSP.160.63

651 Berger, A. & Stünitz, H. (1996) Deformation mechanisms and reaction of hornblende:
652 Examples from the Bergell tonalite (Central Alps). *Tectonophysics*, **257**, 149–174.
653 doi:10.1016/0040-1951(95)00125-5

654 Biermann, C. & Roermund, H.L.M. van. (1983) Defect structures in naturally deformed
655 clinoamphiboles - a TEM study. *Tectonophysics*, **95**, 267–278.

656 Brodie, K.H. & Rutter, E.H. (1985) On the relationship between deformation and
657 metamorphism, with special reference to the behavior of basic rocks. *Metamorph.*
658 *React. Kinet. Textures, Deform.*, 138–179. doi:10.1007/978-1-4612-5066-1_6

659 Bystricky, M. & Mackwell, S. (2001) Creep of dry clinopyroxene aggregates with deformation
660 in the dislocation creep. *J. Geophys. Res.*, **106**, 13443–13454.

661 Connolly, J.A.D. (2009) The geodynamic equation of state: What and how. *Geochemistry,*
662 *Geophys. Geosystems*, **10**. doi:10.1029/2009GC002540

663 Connolly, J.A.D. & Kerrick, D.M. (1987) An algorithm and computer program for calculating
664 composition phase diagrams. *Calphad*, **11**, 1–55. doi:10.1016/0364-5916(87)90018-6

665 Corfu, F., Gasser, D. & Chew, D.M. (2014) New perspectives on the caledonides of
666 scandinavia and related areas: Introduction. *Geol. Soc. Spec. Publ.*, **390**, 1–8.
667 doi:10.1144/SP390.28

668 Corfu, F., Torsvik, T.H., Andersen, T.B., Ashwal, L.D., Ramsay, D.M. & Roberts, R.J. (2006)
669 Early Silurian mafic-ultramafic and granitic plutonism in contemporaneous flysch,
670 Magerøy, northern Norway: U-Pb ages and regional significance. *J. Geol. Soc. London.*,
671 **163**, 291–301. doi:10.1144/0016-764905-014

672 Cumbest, R.J., Drury, M.R., Roermund, H.L.M. van & Simpson, C. (1989) Dynamic
673 recrystallization and chemical evolution of clinoamphibole from Senja, Norway. *Contrib.*
674 *to Mineral. Petrol.*, **101**, 339–349. doi:10.1007/BF00375318

675 Díaz Aspiroz, M., Lloyd, G.E. & Fernández, C. (2007) Development of lattice preferred
676 orientation in clinoamphiboles deformed under low-pressure metamorphic conditions.
677 A SEM/EBSD study of metabasites from the Aracena metamorphic belt (SW Spain). *J.*
678 *Struct. Geol.*, **29**, 629–645. doi:10.1016/j.jsg.2006.10.010

679 Dimanov, A., Dresen, G., Xiao, X. & Wirth, R. (1999) Grain boundary diffusion creep of
680 synthetic anorthite aggregates: The effect of water. *J. Geophys. Res. Solid Earth*, **104**,
681 10483–10497. doi:10.1029/1998jb900113

682 Dimanov, A. & Dresen, G. (2005) Rheology of synthetic anorthite-diopside aggregates:
683 Implications for ductile shear zones. *J. Geophys. Res. Solid Earth*, **110**, 1–24.
684 doi:10.1029/2004JB003431

685 Dimanov, A., Lavie, M.P., Dresen, G., Ingrin, J. & Jaoul, O. (2003) Creep of polycrystalline
686 anorthite and diopside. *J. Geophys. Res. Solid Earth*, **108**. doi:10.1029/2002jb001815

687 Dimanov, Alexandre, Raphanel, J. & Dresen, G. (2011) Newtonian flow of heterogeneous
688 synthetic gabbros at high strain: Grain sliding, ductile failure, and contrasting local
689 mechanisms and interactions. *Eur. J. Mineral.*, **23**, 303–322. doi:10.1127/0935-

1221/2011/0023-2110

Dollinger, G. & Blacic, J.D. (1975) Deformation mechanisms in experimentally and naturally deformed amphiboles. *Earth Planet. Sci. Lett.*, **26**, 409–416. doi:10.1016/0012-821X(75)90016-3

Elliott, D. (1973) Diffusion flow laws in metamorphic rocks. *Bull. Geol. Soc. Am.*, **84**, 2645–2664. doi:10.1130/0016-7606(1973)84<2645:DFLIMR>2.0.CO;2

Elyaszadeh, R., Prior, D.J., Sarkarinejad, K. & Mansouri, H. (2018) Different slip systems controlling crystallographic preferred orientation and intracrystalline deformation of amphibole in mylonites from the Neyriz mantle diapir, Iran. *J. Struct. Geol.*, **107**, 38–52, Elsevier. doi:10.1016/j.jsg.2017.11.020

Faber, C., Stünitz, H., Gasser, D., Jeřábek, P., Kraus, K., Corfu, F., Ravna, E.K., *et al.* (2019) Anticlockwise metamorphic pressure-Temperature paths and nappe stacking in the Reisa Nappe Complex in the Scandinavian Caledonides, northern Norway: Evidence for weakening of lower continental crust before and during continental collision. *Solid Earth*, **10**, 117–148. doi:10.5194/se-10-117-2019

Gasser, D., Jeřábek, P., Faber, C., Stünitz, H., Menegon, L., Corfu, F., Erambert, M., *et al.* (2015) Behaviour of geochronometers and timing of metamorphic reactions during deformation at lower crustal conditions: Phase equilibrium modelling and U-Pb dating of zircon, monazite, rutile and titanite from the Kalak Nappe Complex, northern Norway. *J. Metamorph. Geol.*, **33**, 513–534. doi:10.1111/jmg.12131

Getsinger, A.J., Hirth, G., Stünitz, H. & Goergen, E.T. (2013) Influence of water on rheology and strain localization in the lower continental crust. *Geochemistry, Geophys.*

712 *Geosystems*, **14**, 2247–2264. doi:10.1002/ggge.20148

713 Green, E.C.R., White, R.W., Diener, J.F.A., Powell, R., Holland, T. & Palin, R.M. (2016)
714 Activity–composition relations for the calculation of partial melting equilibria in
715 metabasic rocks. *J. Metamorph. Geol.*, **34**, 845–869. doi:10.1111/jmg.12211

716 Hacker, B.R. & Christie, J.M. (1990) Brittle/ductile and plastic/cataclastic transitions in
717 experimentally deformed and metamorphosed amphibolite. *Geophys. Monogr.*, **56**,
718 127–147.

719 Handy, M.R. & Stünitz, H. (2002) Strain localization by fracturing and reaction weakening -A
720 mechanism for initiating exhumation of subcontinental mantle beneath rifted margins.
721 *Geol. Soc. Spec. Publ.*, **200**, 387–407. doi:10.1144/GSL.SP.2001.200.01.22

722 Holland, T. & Blundy, J. (1994) Non-ideal interactions in calcic amphiboles and their bearing
723 on amphibole-plagioclase thermometry. *Contrib. to Mineral. Petrol.*, **116**, 433–447.
724 doi:10.1007/BF00310910

725 Holland, T. & Powell, R. (2003) Activity-compositions relations for phases in petrological
726 calculations: An asymetric multicomponent formulation. *Contrib. to Mineral. Petrol.*,
727 **145**, 492–501. doi:10.1007/s00410-003-0464-z

728 Holland, T. & Powell, R. (2011) An improved and extended internally consistent
729 thermodynamic dataset for phases of petrological interest, involving a new equation of
730 state for solids. *J. Metamorph. Geol.*, **29**, 333–383. doi:10.1111/j.1525-
731 1314.2010.00923.x

732 Imon, R., Okudaira, T. & Fujimoto, A. (2002) Dissolution and precipitation processes in
733 deformed amphibolites: An example from the ductile shear zone of the Ryoke

734 metamorphic belt, SW Japan. *J. Metamorph. Geol.*, **20**, 297–308. doi:10.1046/j.1525-
735 1314.2002.00367.x

736 Imon, R., Okudaira, T. & Kanagawa, K. (2004) Development of shape- and lattice-preferred
737 orientations of amphibole grains during initial cataclastic deformation and subsequent
738 deformation by dissolution-precipitation creep in amphibolites from the Ryoke
739 metamorphic belt, SW Japan. *J. Struct. Geol.*, **26**, 793–805.
740 doi:10.1016/j.jsg.2003.09.004

741 Ji, S., Shao, T., Michibayashi, K., Long, C., Wang, Q., Kondo, Y., Zhao, W., *et al.* (2013) A new
742 calibration of seismic velocities, anisotropy, fabrics, and elastic moduli of amphibole-
743 rich rocks. *J. Geophys. Res. E Planets*, **118**, 4699–4728. doi:10.1002/jgrb.50352

744 Kanagawa, K., Shimano, H. & Hiroi, Y. (2008) Mylonitic deformation of gabbro in the lower
745 crust: A case study from the Pankenushi gabbro in the Hidaka metamorphic belt of
746 central Hokkaido, Japan. *J. Struct. Biol.*, **30**, 1150–1166. doi:10.1016/j.jsg.2008.05.007

747 Kim, J. & Jung, H. (2019) New Crystal Preferred Orientation of Amphibole Experimentally
748 Found in Simple Shear. *Geophys. Res. Lett.*, **46**, 12996–13005.
749 doi:10.1029/2019GL085189

750 Ko, B. & Jung, H. (2015) Crystal preferred orientation of an amphibole experimentally
751 deformed by simple shear. *Nat. Commun.*, **6**, Nature Publishing Group.
752 doi:10.1038/ncomms7586

753 Kruse, R. & Stünitz, H. (1999) Deformation mechanisms and phase distribution in mafic high-
754 temperature mylonites from the Jotun Nappe, southern Norway. *Tectonophysics*, **303**,
755 223–249. doi:10.1016/S0040-1951(98)00255-8

Kruse, R., Stünitz, H. & Kunze, K. (2001) Dynamic recrystallization processes in plagioclase porphyroclasts. *J. Struct. Geol.*, **23**, 1781–1802. doi:10.1016/S0191-8141(01)00030-X

Langdon, T.G. (2006) Grain boundary sliding revisited: Developments in sliding over four decades. *J. Mater. Sci.*, **41**, 597–609. doi:10.1007/s10853-006-6476-0

Lapworth, T., Wheeler, J. & Prior, D.J. (2002) The deformation of plagioclase investigated using electron backscatter diffraction crystallographic preferred orientation data. *J. Struct. Geol.*, **24**, 387–399. doi:10.1016/S0191-8141(01)00057-8

Leake, B.E., Woolley, A.R., Arps, C.E.S., Birch, W.D., Gilbert, M.C., Grice, J.D., Hawthorne, F.C., *et al.* (1997) Nomenclature of amphiboles: Report of the subcommittee on amphiboles of the international mineralogical association, commission on new minerals and mineral names. *Can. Mineral.*, **35**, 219–246.

Lindahl, I., Stevens, B.P.J. & Zwaan, K.B. (2005) The geology of the Váddás area, Troms: a key to our understanding of the Upper Allochthon in the Caledonides of northern Norway. *Norges Geol. undersøkelse-Bulletin*, **445**, 5–43.

Lloyd, G.E., Butler, R.W.H., Casey, M., Tatham, D.J. & Mainprice, D. (2011) Constraints on the seismic properties of the middle and lower continental crust. *Geol. Soc. Spec. Publ.*, **360**, 7–32. doi:10.1144/SP360.2

Mainprice, D. & Nicolas, A. (1989) Development of shape and lattice preferred orientations: application to the seismic anisotropy of the lower crust. *J. Struct. Geol.*, **11**, 175–189. doi:10.1016/0191-8141(89)90042-4

Mansard, N., Stünitz, H., Raimbourg, H. & Précigout, J. (2020a) The role of deformation-reaction interactions to localize strain in polymineralic rocks : Insights from

778 experimentally deformed plagioclase-pyroxene assemblages, **134**.
779 doi:10.1016/j.jsg.2020.104008

780 Mansard, N., Stünitz, H., Raimbourg, H., Précigout, J., Plunder, A. & Nègre, L. (2020b)
781 Relationship between microstructures and resistance in mafic assemblages that deform
782 and transform. *Solid Earth*, **11**, 2141–2167. doi:10.5194/se-11-2141-2020

783 Marshall, D.B. & McLaren, A.C. (1977) Elastic twinning in experimentally deformed
784 plagioclase feldspars. *Phys. Chem. Miner.*, **41**, 231–240. doi:10.1002/pssa.2210410128

785 Marti, S., Stünitz, H., Heilbronner, R., Plümper, O. & Drury, M. (2017) Experimental
786 investigation of the brittle-viscous transition in ma fi c rocks – Interplay between
787 fracturing , reaction , and viscous deformation. *J. Struct. Geol.*, **105**, 62–79, Elsevier.
788 doi:10.1016/j.jsg.2017.10.011

789 Marti, S., Stünitz, H., Heilbronner, R., Plümper, O. & Kilian, R. (2018) Syn-kinematic hydration
790 reactions, grain size reduction, and dissolution-precipitation creep in experimentally
791 deformed plagioclase-pyroxene mixtures. *Solid Earth*, **9**, 985–1009. doi:10.5194/se-9-
792 985-2018

793 Mauler, A., Bystricky, M., Kunze, K. & Mackwell, S. (2000) Microstructures and lattice
794 preferred orientations in experimentally deformed clinopyroxene aggregates. *J. Struct.*
795 *Geol.*, **22**, 1633–1648. doi:10.1016/S0191-8141(00)00073-0

796 McNamara, D.D., Wheeler, J., Pearce, M.A. & Prior, D.J. (2012) Fabrics produced mimetically
797 during static metamorphism in retrogressed eclogites from the Zermatt-Saas zone,
798 Western Italian Alps. *J. Struct. Geol.*, **44**, 167–178, Elsevier Ltd.
799 doi:10.1016/j.jsg.2012.08.006

800 Mehl, L. & Hirth, G. (2008) Plagioclase preferred orientation in layered mylonites: Evaluation
801 of flow laws for the lower crust. *J. Geophys. Res. Solid Earth*, **113**, 1–19.
802 doi:10.1029/2007JB005075

803 Miranda, E.A., Hirth, G. & John, B.E. (2016) Microstructural evidence for the transition from
804 dislocation creep to dislocation-accommodated grain boundary sliding in naturally
805 deformed plagioclase. *J. Struct. Geol.*, **92**, 30–45, Elsevier Ltd.
806 doi:10.1016/j.jsg.2016.09.002

807 Moghadam, H.S., Stern, R.J. & Rahgoshay, M. (2010) The Dehshir ophiolite (central Iran):
808 Geochemical constraints on the origin and evolution of the inner Zagros ophiolite belt.
809 *Bull. Geol. Soc. Am.*, **122**, 1516–1547. doi:10.1130/B30066.1

810 Molina, J.F., Moreno, J.A., Castro, A., Rodríguez, C. & Fershtater, G.B. (2015) Calcic
811 amphibole thermobarometry in metamorphic and igneous rocks: New calibrations
812 based on plagioclase/amphibole Al-Si partitioning and amphibole/liquid Mg
813 partitioning. *Lithos*, **232**, 286–305, Elsevier B.V. doi:10.1016/j.lithos.2015.06.027

814 Morrison-Smith, D.J. (1976) Transmission electron microscopy of experimentally deformed
815 hornblende. *Am. Mineral.*, **61**, 272–280. doi:10.1144/gsjgs.132.3.0343

816 Nyman, M.W., Law, R.D. & Smelik, E.A. (1992) Cataclastic deformation mechanism for the
817 development of core-mantle structures in amphibole. *Geology*, **20**, 455–458.
818 doi:10.1130/0091-7613(1992)020<0455:CDMFTD>2.3.CO;2

819 Okudaira, T., Jeřábek, P., Stünitz, H. & Fusseis, F. (2015) High-temperature fracturing and
820 subsequent grain-size- sensitive creep in lower crustal gabbros: Evidence for coseismic
821 loading followed by creep during decaying stress in the lower crust? *J. Geophys. Res.*

Solid Earth, **120**, 3119–3141. doi:doi:10.1002/ 2014JB011708

Pearce, M.A., Wheeler, J. & Prior, D.J. (2011) Relative strength of mafic and felsic rocks during amphibolite facies metamorphism and deformation. *J. Struct. Geol.*, **33**, 662–675, Elsevier Ltd. doi:10.1016/j.jsg.2011.01.002

Poirier, J.P. (1985) *Creep of Crystals*, Cambridge University Press. doi:https://doi.org/10.1017/CBO9780511564451

Powell, R. (1985) Regression diagnostics and robust regression in geothermometer/geobarometer calibration: the garnet- clinopyroxene geothermometer revisited. *J. Metamorph. Geol.*, **3**, 231–243. doi:https://doi.org/10.1111/j.1525-1314.1985.tb00319.x

Roberts, D. & Sturt, B.A. (1980) Caledonian deformation in Norway. *J. Geol. Soc. London.*, **137**, 241–250. doi:10.1144/gsjgs.137.3.0241

Rooney, T.P., Riecker, R.E. & Gavasci, A.T. (1975) Hornblende deformation features. *Geology*, **3**, 364–366.

Rooney, T.P., Riecker, R.E. & Ross, M. (1970) Deformation Twins in Hornblende. *Science (80-.).*, **169**, 173–175. doi:10.1126/science.169.3941.173

Rudnick, R.L. & Fountain, D.M. (1995) Nature and composition of the continental crust: a lower crustal perspective. *Rev. Geophys.*, **33**, 267–309. doi:10.1029/95rg01302

Rutter, E.H. (1983) Pressure solution in nature, theory and experiment. *J. Geol. Soc. London.*, **140**, 725–740. doi:10.1144/gsjgs.140.5.0725

Rybacki, E. & Dresen, G. (2004) Deformation mechanism maps for feldspar rocks.

Tectonophysics, **382**, 173–187. doi:10.1016/j.tecto.2004.01.006

Shannon, R.D. & Rossi, R.C. (1964) Definition of Topotaxy. *Nature*, **202**, 1001–1003. doi:10.1038/2021001a0

Siegesmund, S., Helming, K. & Kruse, R. (1994) Complete texture analysis of a deformed amphibolite: comparison between neutron diffraction and U-stage data. *J. Struct. Geol.*, **16**, 131–142. doi:10.1016/0191-8141(94)90024-8

Skrotzki, W. (1992) Defect structure and deformation mechanisms in naturally deformed hornblende. *Phys. Status Solidi*, **131**, 605–624. doi:10.1002/pssa.2211310232

Soret, M., Agard, P., Ildefonse, B., Dubacq, B., Prigent, C. & Rosenberg, C. (2019) Deformation mechanisms in mafic amphibolites and granulites: record from the Semail metamorphic sole during subduction infancy. *Solid Earth Discuss.*, 1–36. doi:10.5194/se-2019-28

Stünitz, H., Fitz Gerald, J.D. & Tullis, J. (2003) Dislocation generation, slip systems, and dynamic recrystallization in experimentally deformed plagioclase single crystals. *Tectonophysics*, **372**, 215–233. doi:10.1016/S0040-1951(03)00241-5

Stünitz, H. (1993) Transition from fracturing to viscous flow in a naturally deformed metagabbro. in *Defects and processes in the solid state: geoscience applications-the MacLaren volume*, pp. 121–150.

Stünitz, H. (1998) Syndeformational recrystallization - dynamic or compositionally induced? *Contrib. to Mineral. Petrol.*, **131**, 219–236.

Stünitz, Holger, Neufeld, K., Heilbronner, R., Finstad, A.K., Konopásek, J. & Mackenzie, J.R. (2020) Transformation weakening: Diffusion creep in eclogites as a result of interaction

865 of mineral reactions and deformation. *J. Struct. Geol.*, **139**.
866 doi:10.1016/j.jsg.2020.104129

867 Tatham, D.J., Lloyd, G.E., Butler, R.W.H. & Casey, M. (2008) Amphibole and lower crustal
868 seismic properties. *Earth Planet. Sci. Lett.*, **267**, 118–128.
869 doi:10.1016/j.epsl.2007.11.042

870 Terry, M.P. & Heidelbach, F. (2006) Deformation-enhanced metamorphic reactions and the
871 rheology of high-pressure shear zones, Western Gneiss Region, Norway. *J. Metamorph.*
872 *Geol.*, **24**, 3–18. doi:10.1111/j.1525-1314.2005.00618.x

873 Tullis, J. (1983) Deformation of feldspars. in *Feldspar mineralogy*, pp. 297–323.

874 Wheeler, J. (1992) Importance of pressure solution and coble creep in the deformation of
875 polymineralic rocks. *J. Geophys. Res. Solid Earth*, **97**, 4579–4586.
876 doi:10.1029/91JB02476

877 White, R.W., Powell, R., Holland, T., Johnson, T.E. & Green, E.C.R. (2014) New mineral
878 activity-composition relations for thermodynamic calculations in metapelitic systems. *J.*
879 *Metamorph. Geol.*, **32**, 261–286. doi:10.1111/jmg.12071

880 Whitney, D.L. & Evans, B.W. (2010) Abbreviations for names of rock-forming minerals. *Am.*
881 *Mineral.*, **95**, 185–187. doi:10.2138/am.2010.3371

882

883

884 **Figures and tables**

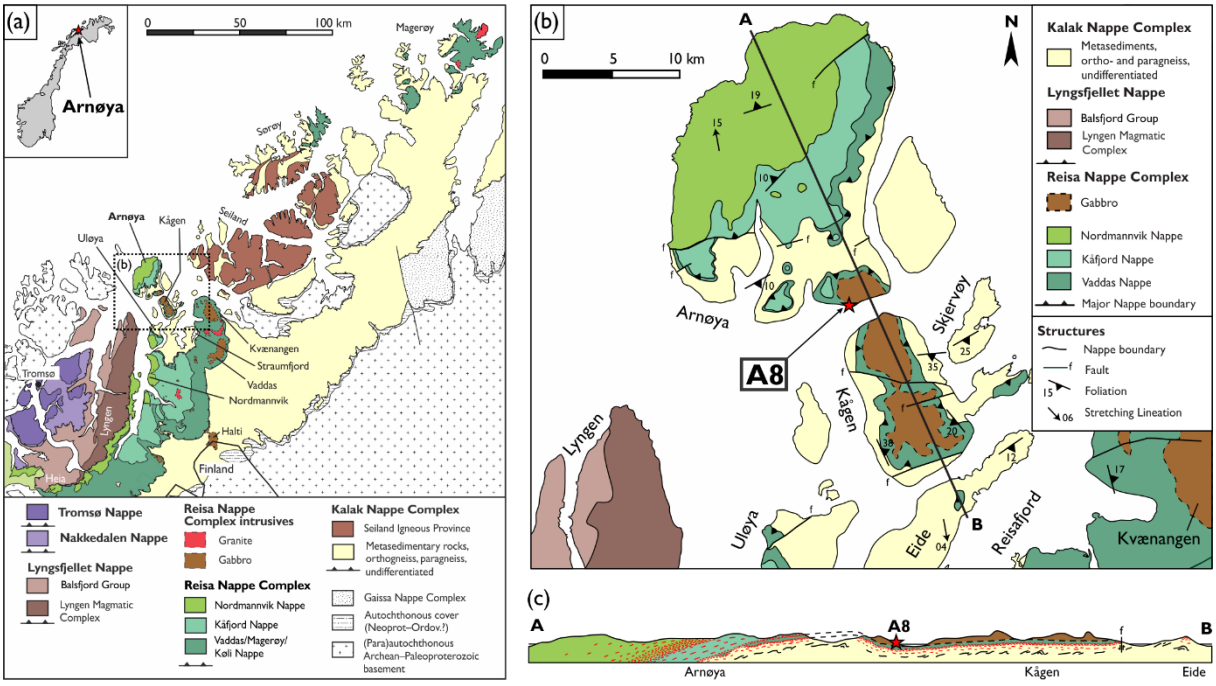

885

886 Figure 1: Geological map of the study area in Northern Norway. (a) North Norwegian Caledonides focussing on the Tromsø
887 to Kalak Nappe Complexes. (b) Detailed map of Arnøya and Kågen to highlight the sample area in the Kågen gabbro. (c) Cross
888 section through Arnøya and Kågen showing the gabbro intruded into the Vaddas Nappe. After Faber et al. (2019).

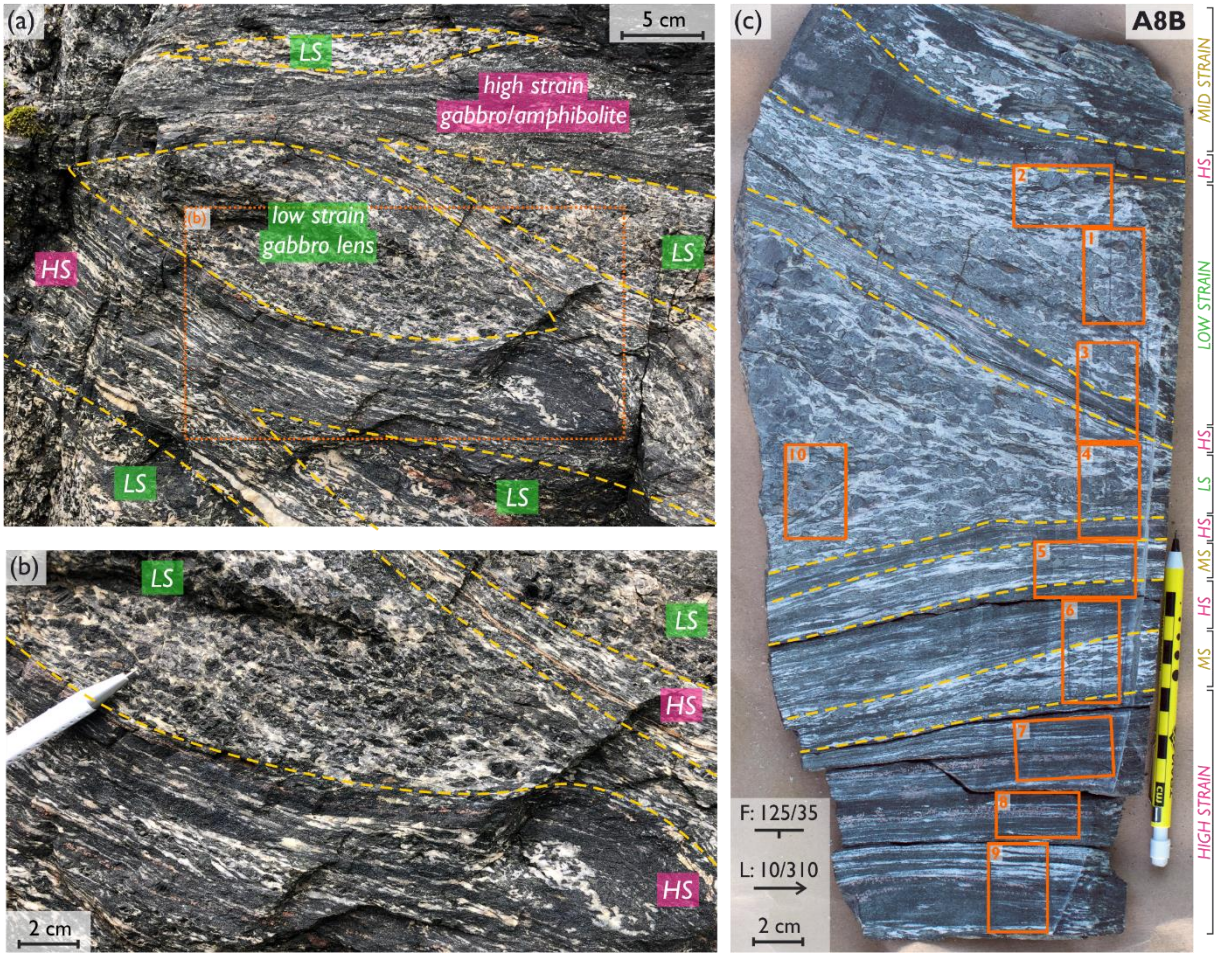

Figure 2: (a) Outcrop photograph of sample area, boundaries between low and high deformation areas highlighted by yellow dashed lines. (b) Detailed photograph from (a) with deformation boundaries and low/high strain zones identified. (c) Photograph of sample A8B with thin section locations highlighted by orange boxes, deformation boundaries between low, mid and high strain zones identified. LS, low strain; MS, mid strain; HS, high strain.

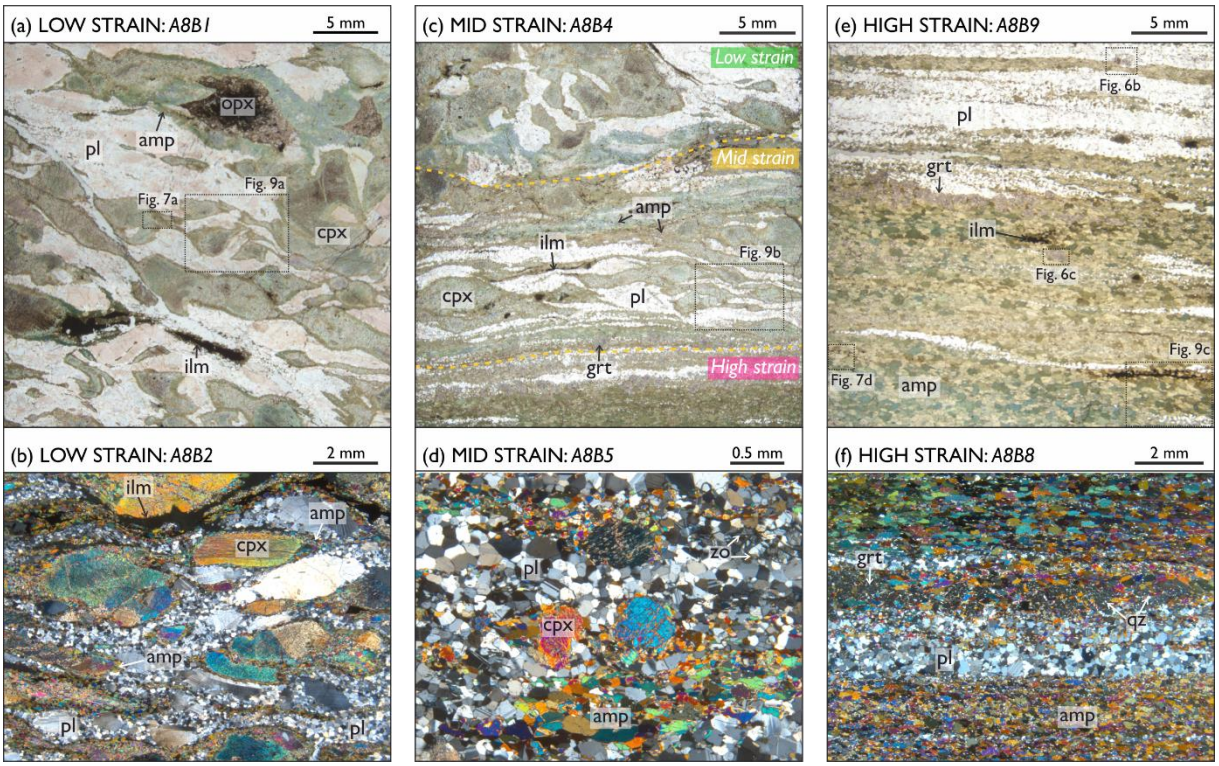

Figure 3: Representative thin section photomicrographs of (a-b) low, (c-d) mid and (e-f) high strain areas in sample A8B. (a, c, e) Photomicrographs in plain polarised light and (b, d, f) under cross-polarised light.

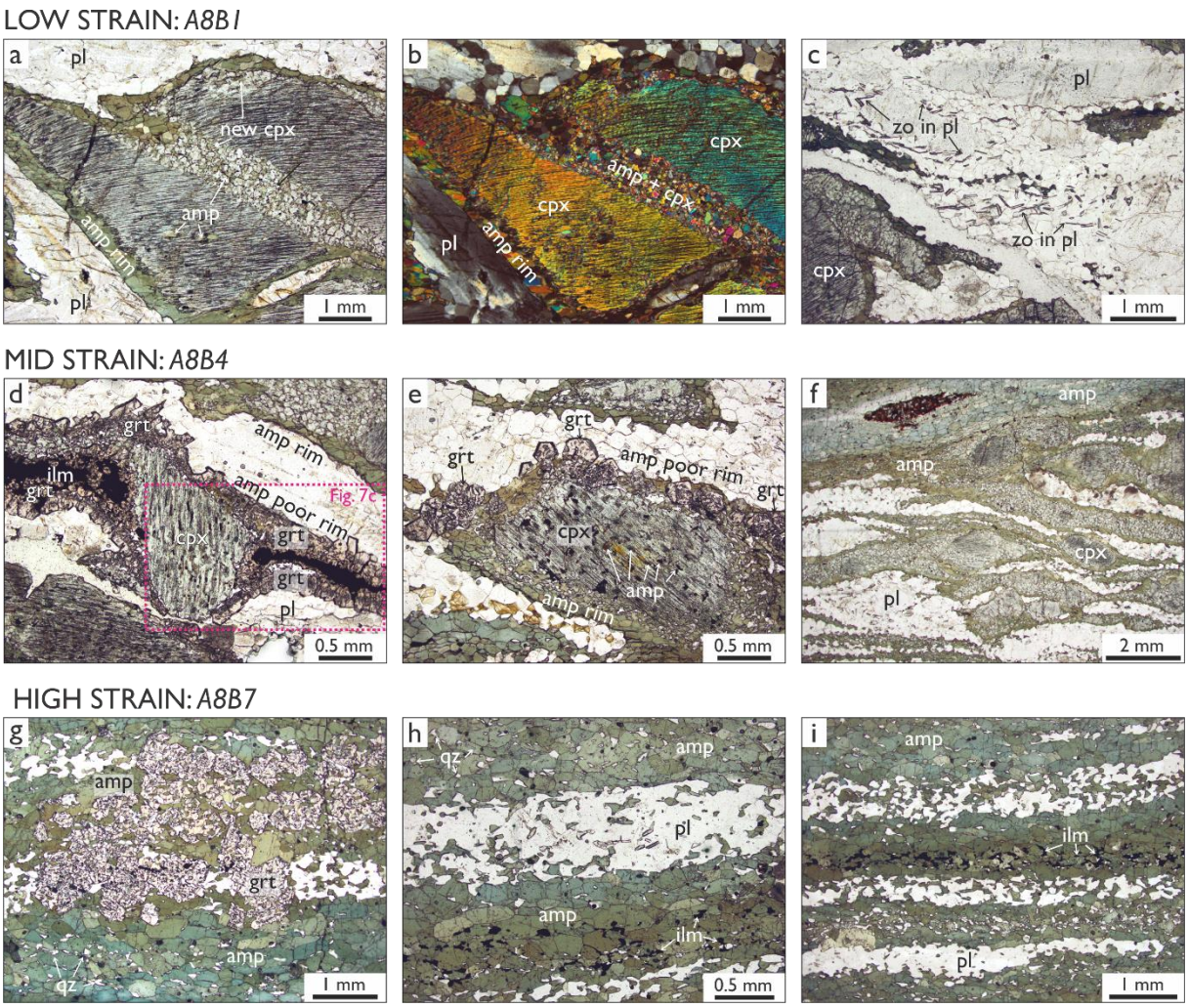

Figure 4: Detailed thin section photomicrographs of specific textures in (a-c) low, (d-f) mid and (g-i) high strain areas in sample A8B. All photomicrographs are in plain polarised light except (b) that is under cross-polarised light.

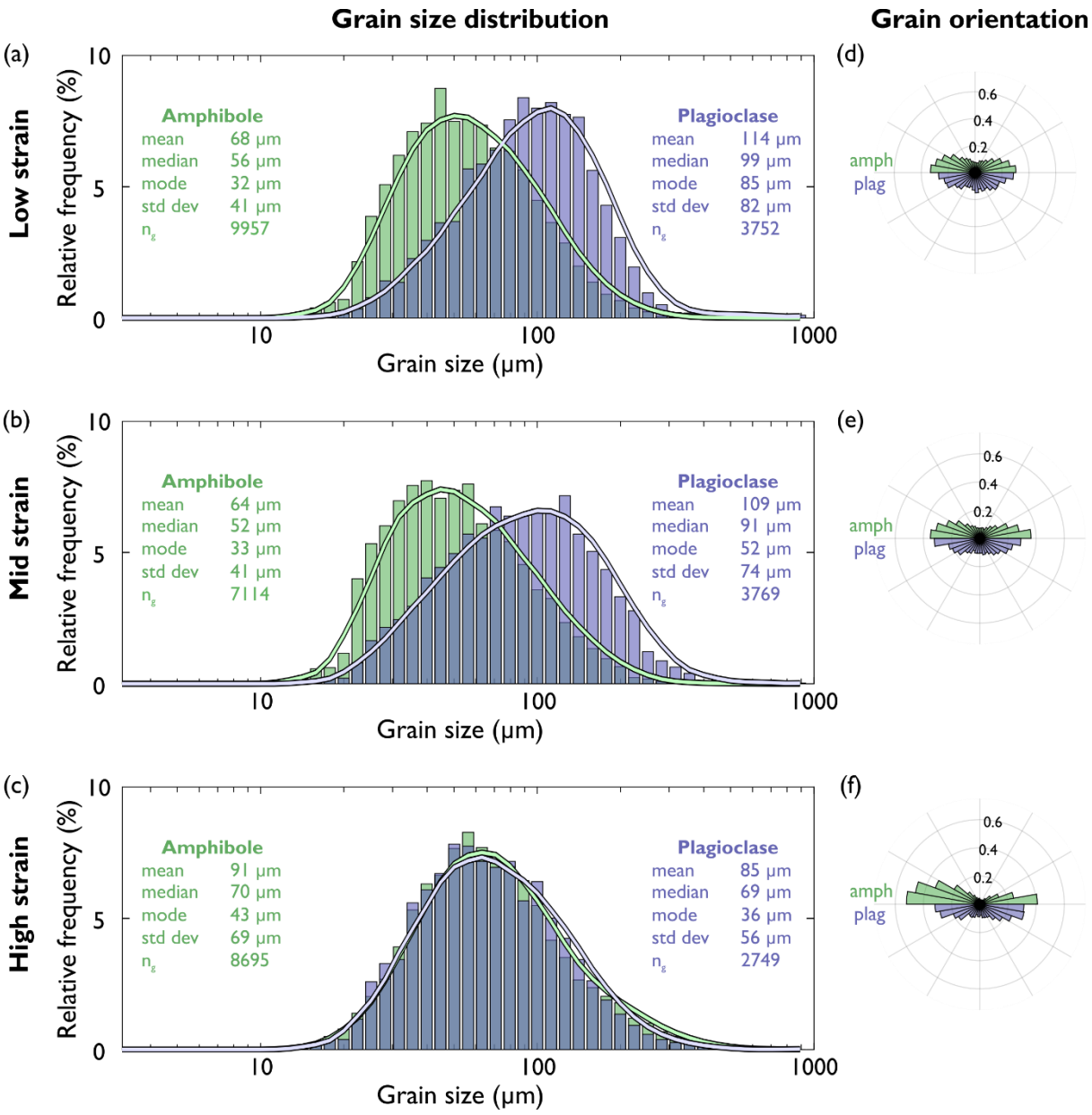

Figure 5: Grain size and shape properties for amphibole and plagioclase grains. (a-c) Log normal grain size distribution for amphibole and plagioclase grains in low to high strain areas of the sample. (d-f) Normalised grain orientation or shape preferred orientation of amphibole and plagioclase grains in low to high strain areas. Number of grains considered for each strain area is indicated by n_g.

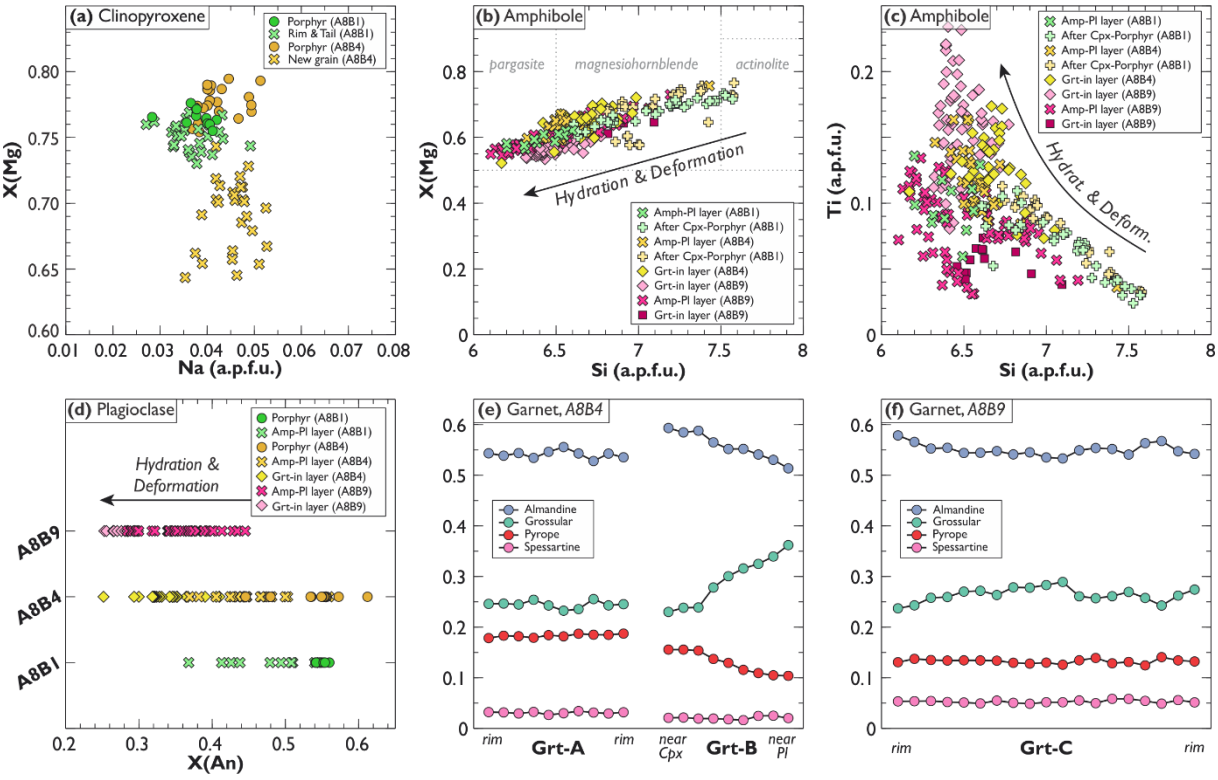

Figure 6: Point analyses and compositions for (a) clinopyroxene, (b-c) amphibole, (d) plagioclase and (e-f) garnet from low (A8B1), mid (A8B4) and high (A8B9) high strain areas of the Kågen gabbro margins.

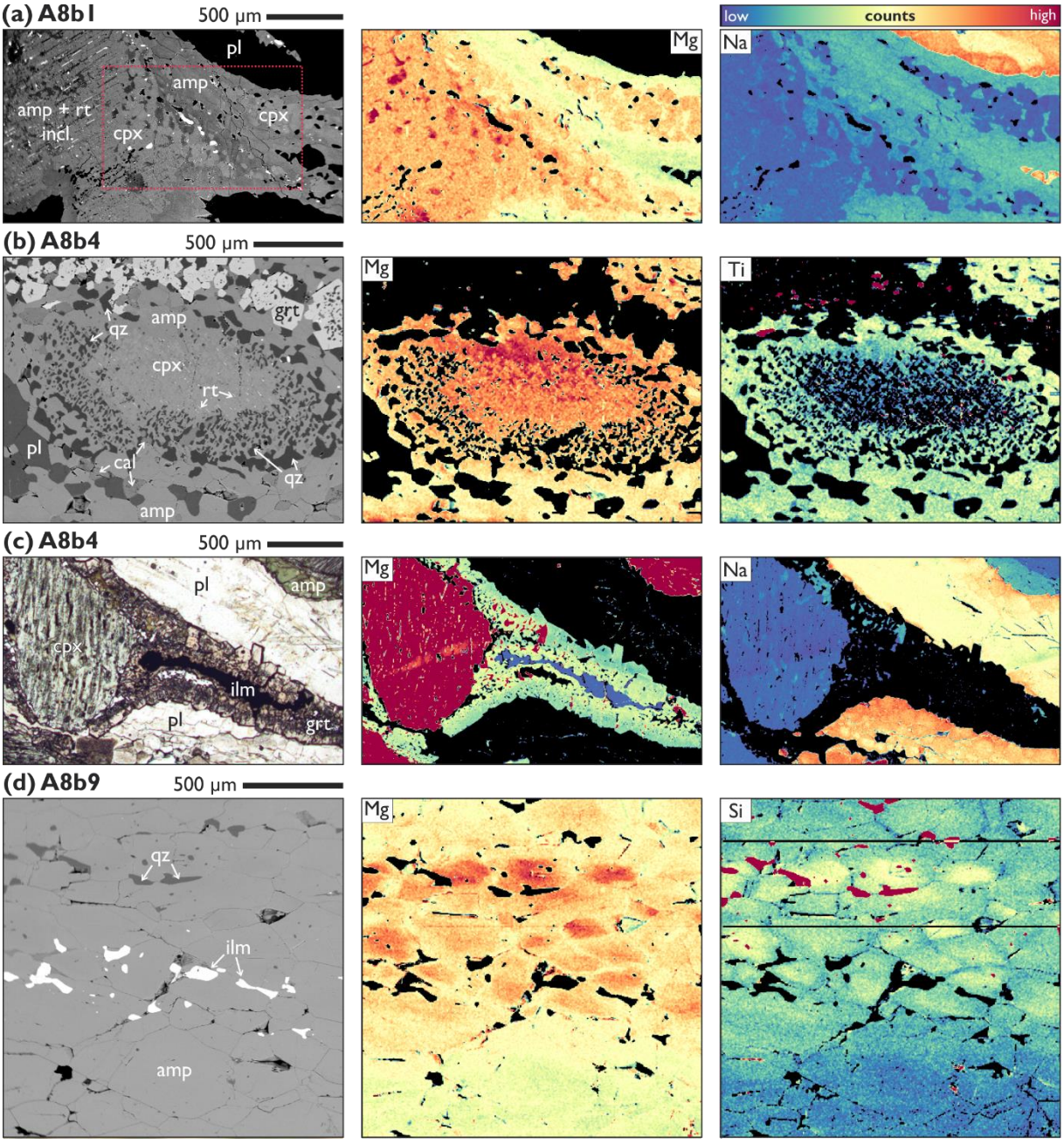

913

914 Figure 7: BSE images (c – photomicrograph) and compositional maps of detailed microstructural features in (a) low, (b-c) mid
915 and (d) high strain areas of the Kågen gabbro margins.

916

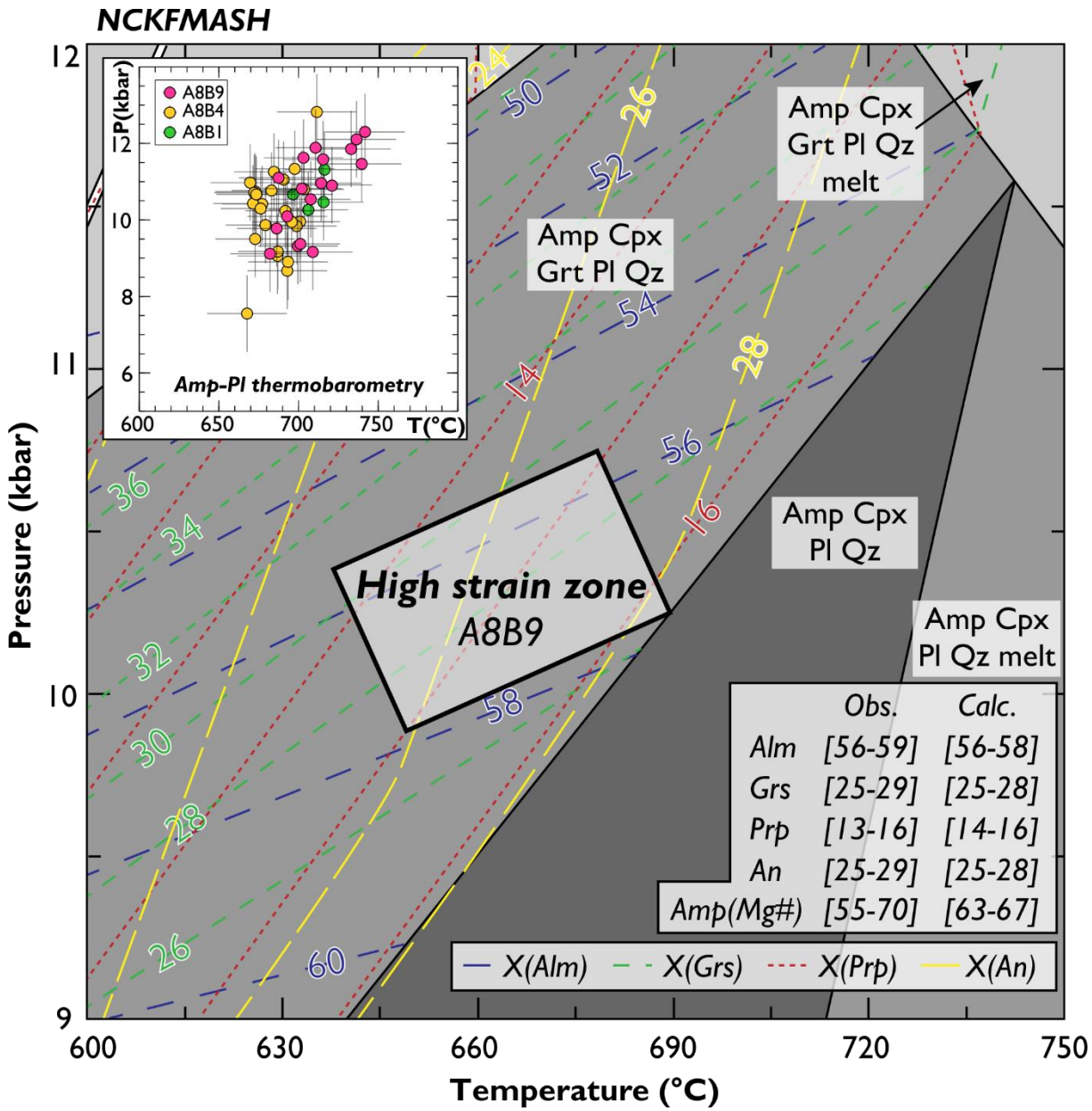

Figure 8: Estimated P-T conditions for the high strain areas of the Kågen gabbro margins. Inset shows amphibole-plagioclase thermobarometry for low, mid and high strain areas. Oxide totals for pseudosection calculation are from a XRF measurements of a high strain area: Na_2O 2.88, MgO 8.27, Al_2O_3 14.11, SiO_2 49.97, CaO 11.49, FeO 8.54, H_2O 1.15.

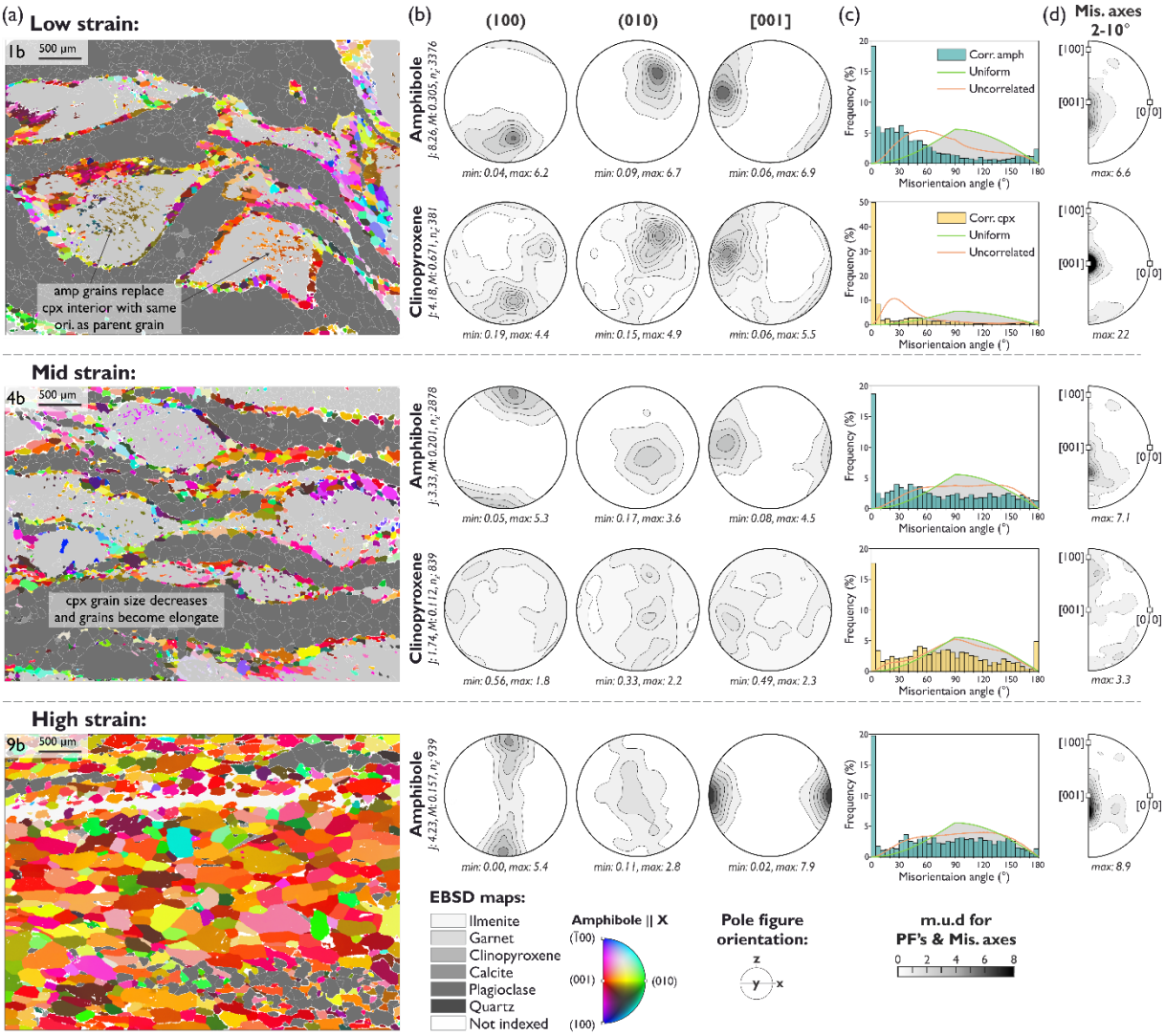

Figure 9: (a) EBSD maps of amphibole orientations coloured parallel to the X direction, all other minerals are shown in grey. All maps are at the same scale to highlight the change in grain size and texture between the differently deformed areas. (b) Pole figures showing amphibole CPO for the low to high strain areas, and clinopyroxene CPO for the low and mid strain areas. Clinopyroxene CPO's are not plotted for the high strain area as there is less than 1% present in the map giving skewed results due to lack of grains. All pole figures are equal area, lower hemisphere projections plotted as point per grain. J-index, M-index and number of grains (n_g) is shown for each set of pole figures. (c) Distribution of misorientation angles between correlated (adjacent) pixels (histogram) and between uncorrelated pixels (orange curve) of amphibole. The uniform (green) curve corresponds to the theoretical misorientation distribution for perfectly randomly oriented crystals. (d) Amphibole and clinopyroxene inverse pole figures showing the distribution of correlated misorientation axes (between 2 and 10°). All contours are multiples of uniform distribution (m.u.d).

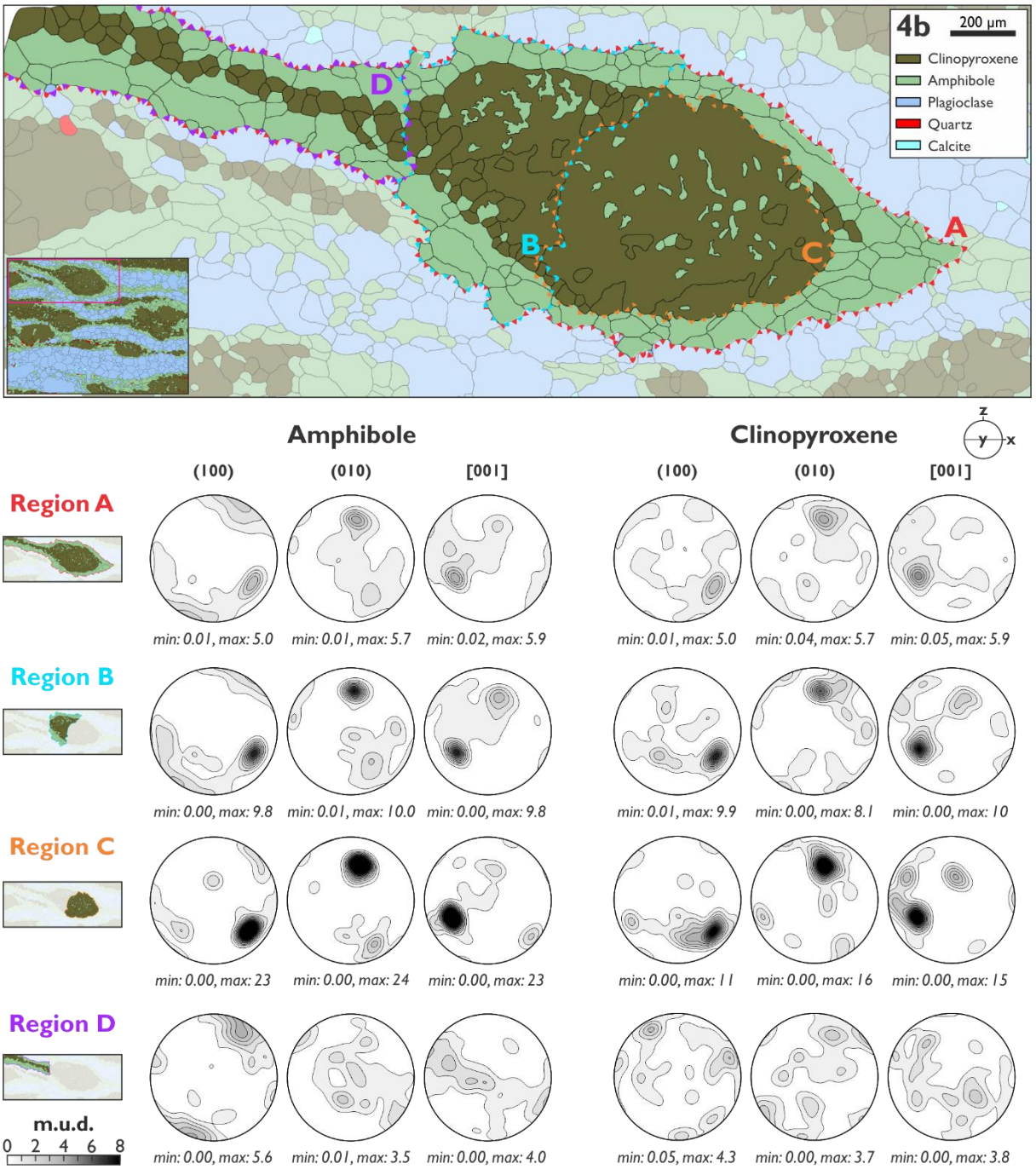

Figure 10: EBSD phase map of a clinopyroxene grain with amphibole corona, below are CPO pole figures for selected regions associated with the clinopyroxene grain. Region A (red) includes the clinopyroxene and all grains that mantle it. Region B (blue) contains the recrystallized portion of the clinopyroxene grain and the amphibole grains that mantle and are included in the clinopyroxene grain. Region C (orange) focusses on the right hand side of the clinopyroxene grain and the amphibole inclusions within the grain. Region D (purple) includes the clinopyroxene and amphibole grains in the recrystallized tail. All pole figures are equal area, lower hemisphere projections plotted as point per grain.

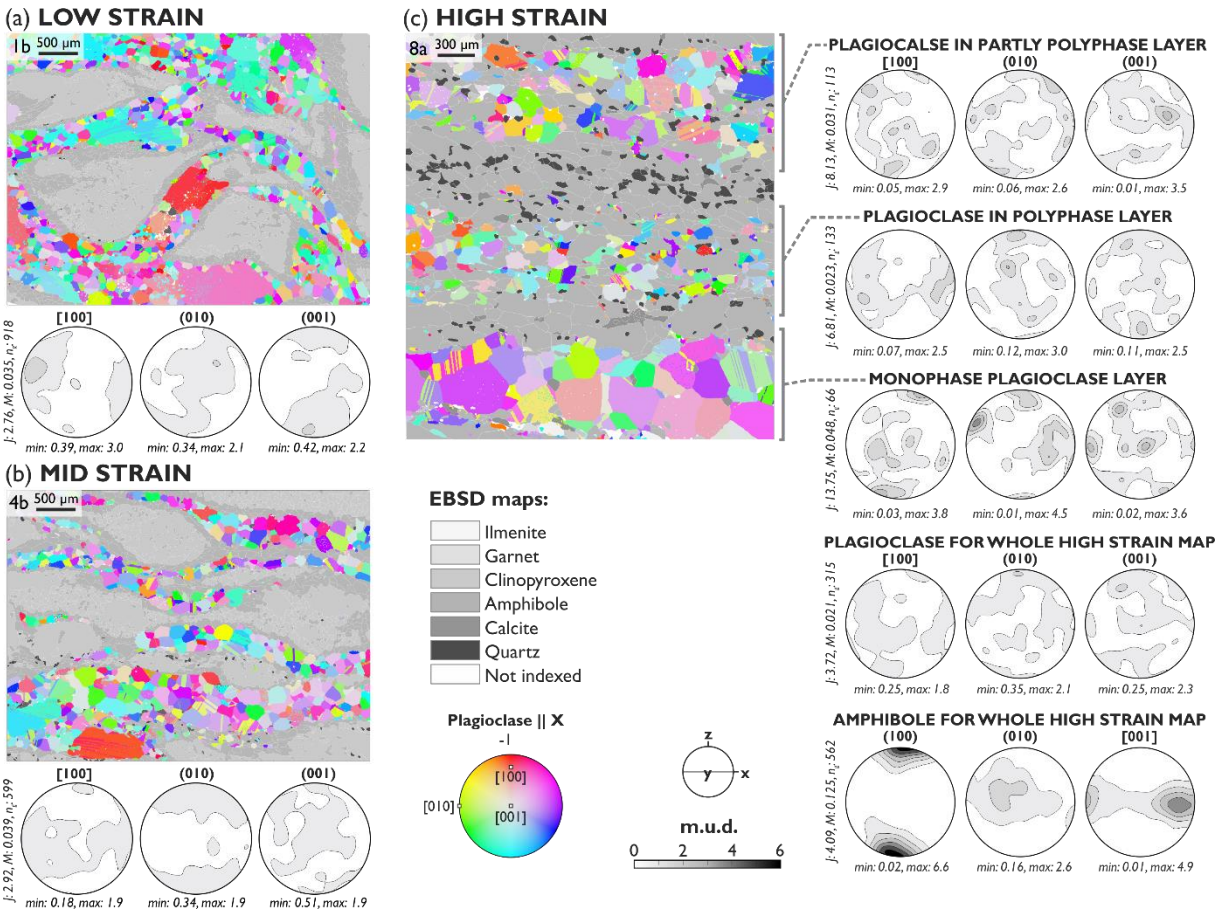

Figure 11: EBSD map and plagioclase CPO pole figures for example (a) low, (b) mid and (c) high strain areas. EBSD maps show plagioclase orientations coloured parallel to the X direction, all other minerals are shown in grey. Pole figures showing plagioclase CPO, for (c), additional CPO are included for polyphase and monophase areas as well as the amphibole whole map CPO is also included (amphibole CPO for a and b are shown in Figure 9). All pole figures are equal area, lower hemisphere projections plotted as point per grain. J-index, M-index and number of grains (n_g) is shown for each set of pole figures.

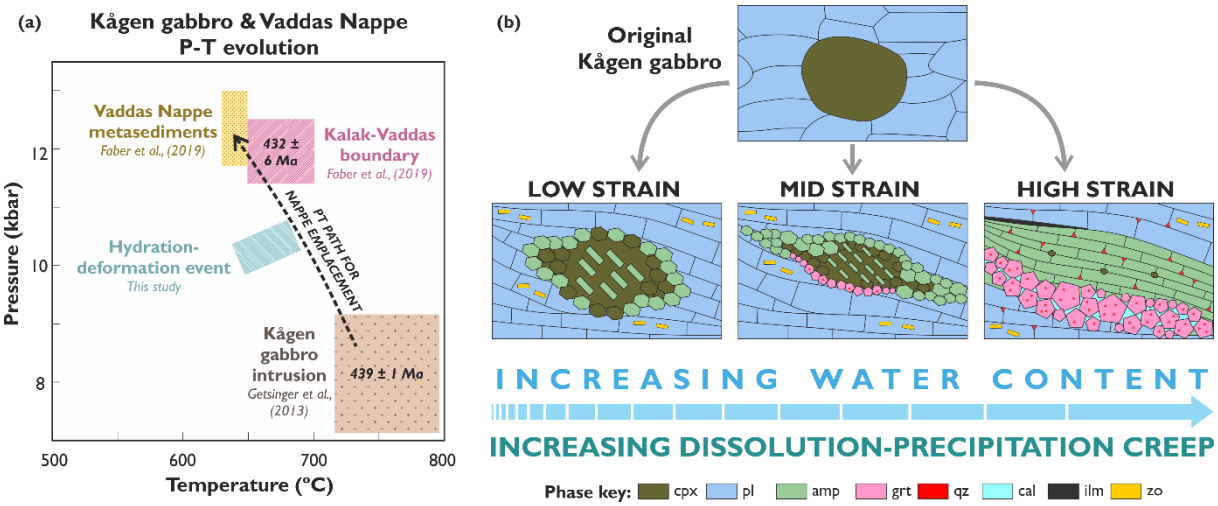

Figure 12: (a) Composite P-T-t evolution of Kågen gabbro and Vaddas Nappe utilising P-T estimates from this study for the hydration-deformation event, Getsinger et al. (2013) for the Kågen gabbro intrusion and Faber et al. (2019) for Vaddas Nappe metasediments and Kalak-Vaddas boundary. (b) Schematic diagram of the microstructural evolution of Kågen gabbro margins when deformation occurred under differing hydration conditions.

Table 1: Selected representative analyses of garnet, clinopyroxene, plagioclase and amphibole from point analysis.

Min.	Grt	Grt	Grt	Cpx	Cpx	Cpx	Cpx	Pl	Pl	Pl	Pl	Pl	Amp	Amp	Amp	Amp
Sample	A8b4	A8b4	A8b9	A8b1	A8b1	A8b4	A8b4	A8b1	A8b1	A8b4	A8b9	A8b9	A8b1	A8b4	A8b4	A8b9
Anal.	256/1	111 /1	125 /6	15/1	87 /1	224/1	92/1	101/8	61 /1	212/1	44 /1	12 /1	60/1	211/1	364/1	119/1
SiO_2	38.15	38.33	38.18	53.94	53.22	53.77	52.45	54.46	58.2	59.24	59.9	62.12	42.1	43.79	52.47	43.34
TiO_2	0.06	0.01	0.06	0.11	0.13	0.10	0.06	0.00	0.00	0.00	0.00	0.00	1.23	1.48	0.34	1.18
Al_2O_3	21.24	20.82	21.06	1.12	1.39	1.18	1.06	29.55	27.36	25.88	25.30	23.83	16.47	13.53	5.48	12.77
FeO	25.01	24.31	25.22	7.13	8.64	6.78	11.22	0.00	0.00	0.00	0.00	0.00	12.85	13.20	9.45	15.37
MnO	1.50	0.95	2.34	0.14	0.25	0.12	0.06	0.00	0.00	0.00	0.00	0.00	0.20	0.04	0.14	0.19
MgO	4.70	2.76	3.50	13.87	13.12	13.95	12.07	0.00	0.00	0.00	0.00	0.00	10.00	11.05	16.49	10.37
CaO	9.28	13.37	9.78	23.39	23.08	23.81	22.37	11.33	8.76	7.68	7.03	5.24	11.49	11.59	11.80	11.07
Na_2O	0.02	0.01	0.00	0.51	0.52	0.57	0.62	5.07	6.50	7.36	7.47	8.51	2.26	2.13	0.81	1.91
K_2O	0.00	0.00	0.04	0.00	0.00	0.00	0.00	0.00	0.05	0.07	0.09	0.06	0.46	0.43	0.09	0.46
Σ	100.0	100.5	100.2	100.2	100.4	100.3	99.9	100.4	100.8	100.2	100.0	99.8	97.1	97.2	97.1	96.7
Ox.	12	12	12	6	6	6	6	8	8	8	8	8	23	23	23	23
Si	2.99	3.01	3.01	1.99	1.98	1.99	1.98	2.44	2.58	2.64	2.67	2.75	6.20	6.44	7.43	6.42
Ti	0.00	0.00	0.00	0.00	0.00	0.00	0.00	0.00	0.00	0.00	0.00	0.00	2.86	2.35	0.91	2.23
Al	1.96	1.92	1.95	0.05	0.06	0.05	0.05	1.56	1.42	1.36	1.33	1.25	0.14	0.16	0.04	0.13
Fe_{tot}	1.64	1.59	1.66	0.22	0.27	0.21	0.35	0.00	0.00	0.00	0.00	0.00	1.58	1.62	1.12	1.90
Mn	0.10	0.06	0.16	0.00	0.01	0.00	0.00	0.00	0.00	0.00	0.00	0.00	0.02	0.01	0.02	0.02
Mg	0.55	0.32	0.41	0.76	0.73	0.77	0.68	0.00	0.00	0.00	0.00	0.00	2.20	2.42	3.48	2.29
Ca	0.78	1.12	0.82	0.93	0.92	0.94	0.91	0.55	0.42	0.37	0.36	0.25	1.81	1.83	1.79	1.76
Na	0.00	0.00	0.00	0.04	0.04	0.04	0.05	0.44	0.56	0.63	0.64	0.73	0.65	0.61	0.22	0.55
K	0.00	0.00	0.00	0.00	0.00	0.00	0.00	0.00	0.00	0.00	0.00	0.00	0.09	0.08	0.02	0.09
Prp	0.18	0.10	0.13	–	–	–	–	–	–	–	–	–	–	–	–	–
Alm	0.53	0.51	0.54	–	–	–	–	–	–	–	–	–	–	–	–	–
Grs	0.25	0.36	0.27	–	–	–	–	–	–	–	–	–	–	–	–	–
Sps	0.03	0.02	0.05	–	–	–	–	–	–	–	–	–	–	–	–	–
Mg#	0.25	0.17	0.20	0.78	0.73	0.79	0.66	–	–	–	–	–	0.58	0.60	0.76	0.55
An#	–	–	–	–	–	–	–	0.56	0.43	0.37	0.36	0.26	–	–	–	–

Abbreviations after Whitney and Evans (2010).

957

958

959 **Supplementary material**

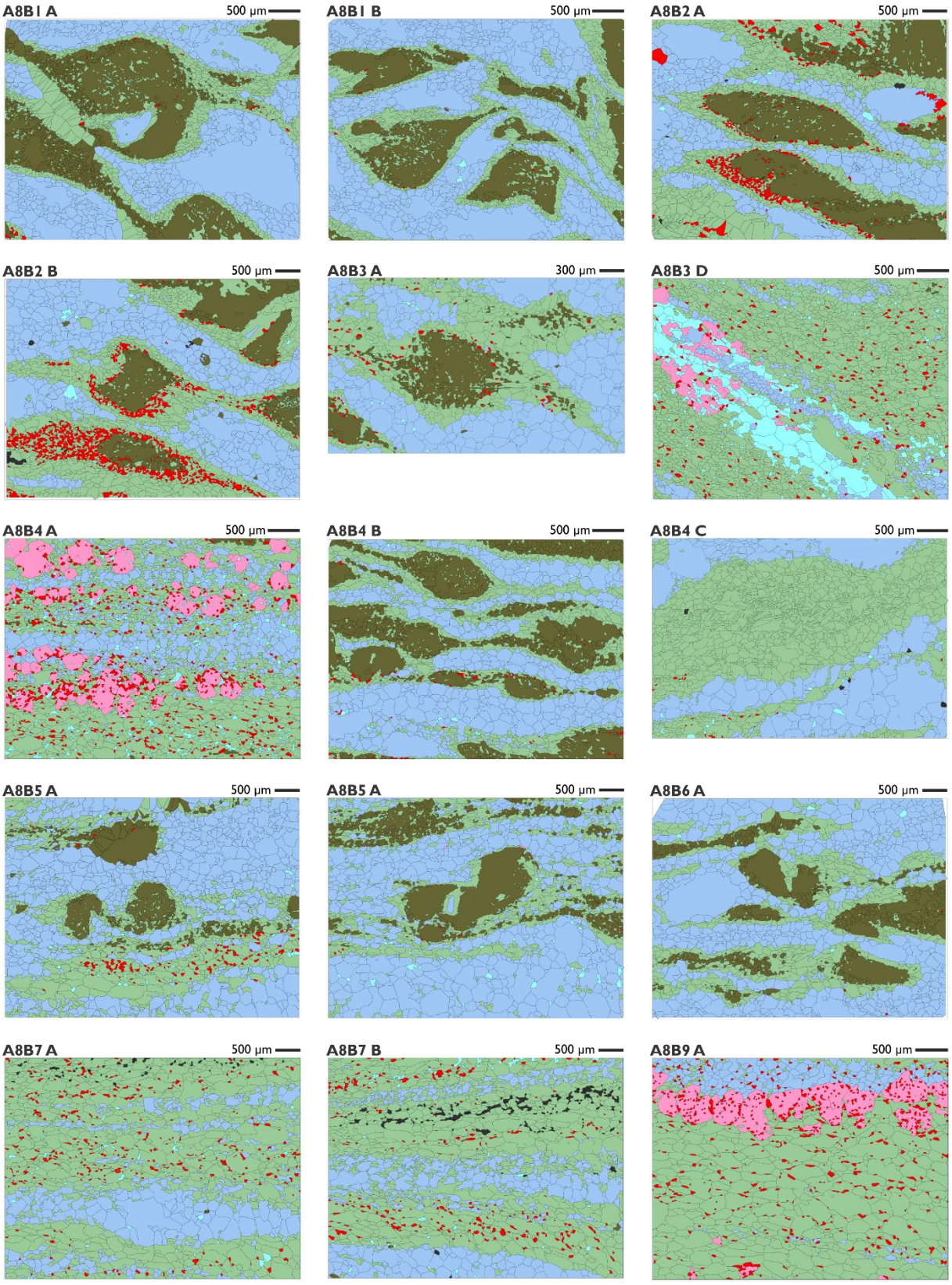

960

961 Figure S1: EBSD phase maps for all datasets used in this study. Data are displayed as grain maps that were calculated within
962 MTEX.

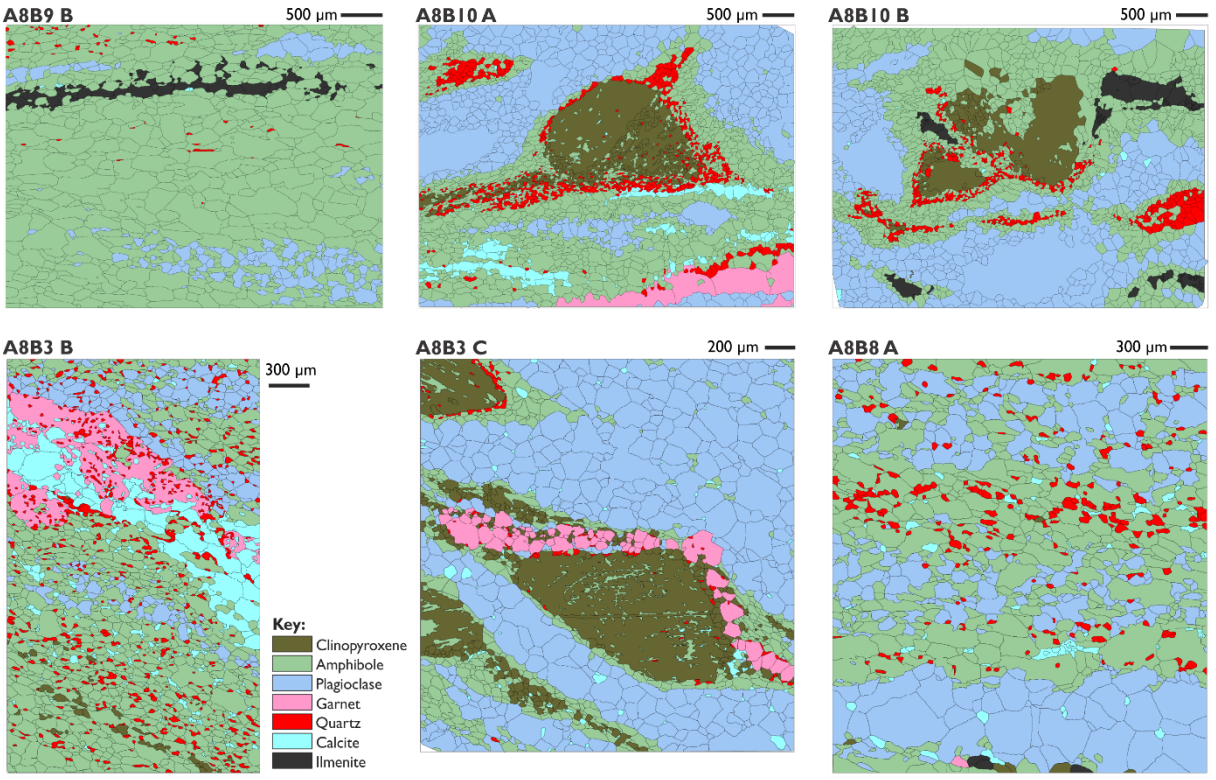

Figure S1 continued.

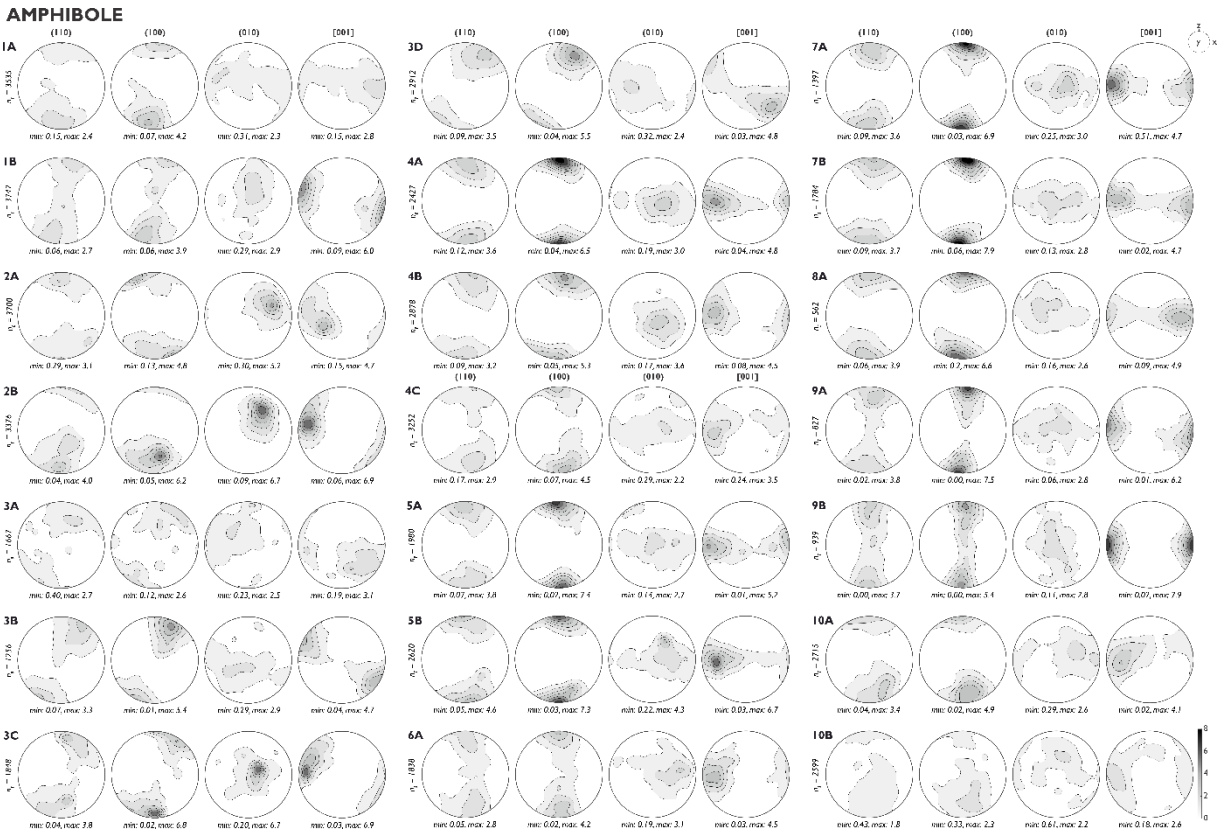

Figure S2: Point per grain, equal area, lower hemisphere amphibole CPO pole figures.

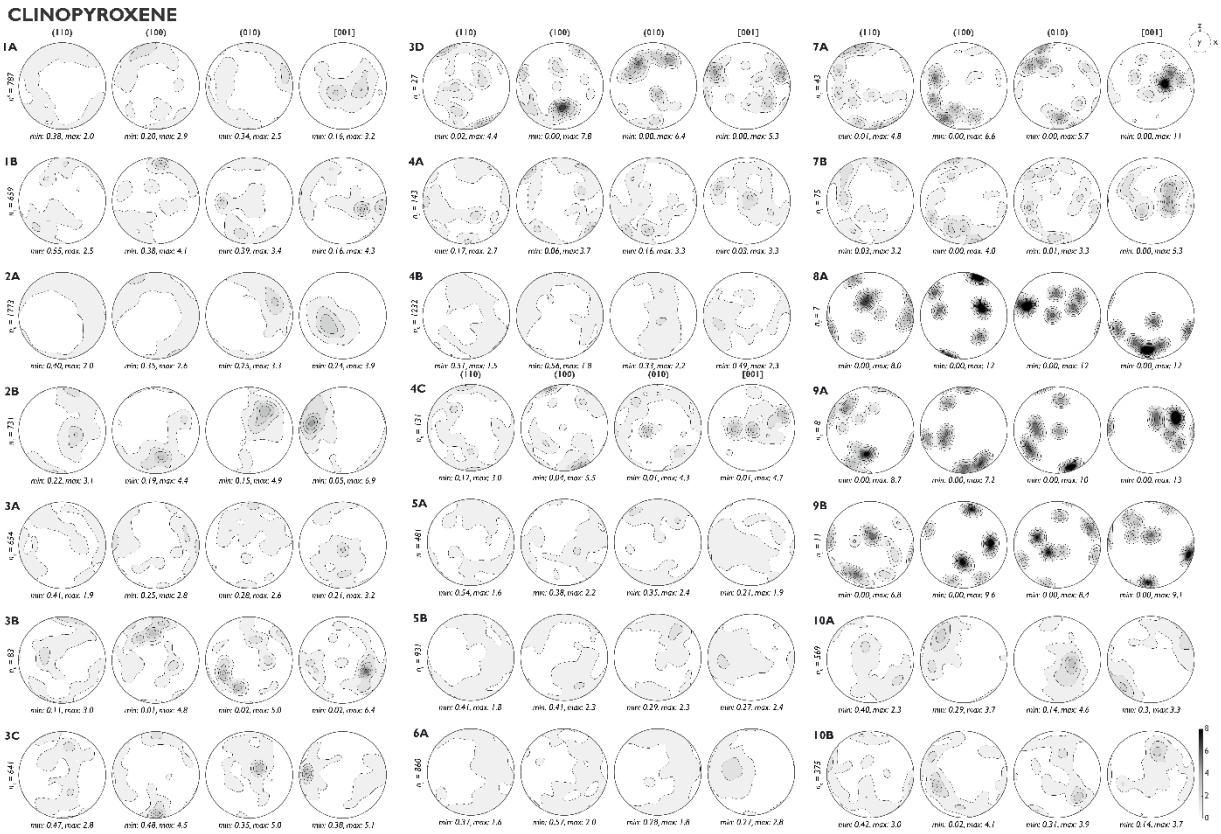

Figure S3: Point per grain, equal area, lower hemisphere clinopyroxene CPO pole figures.

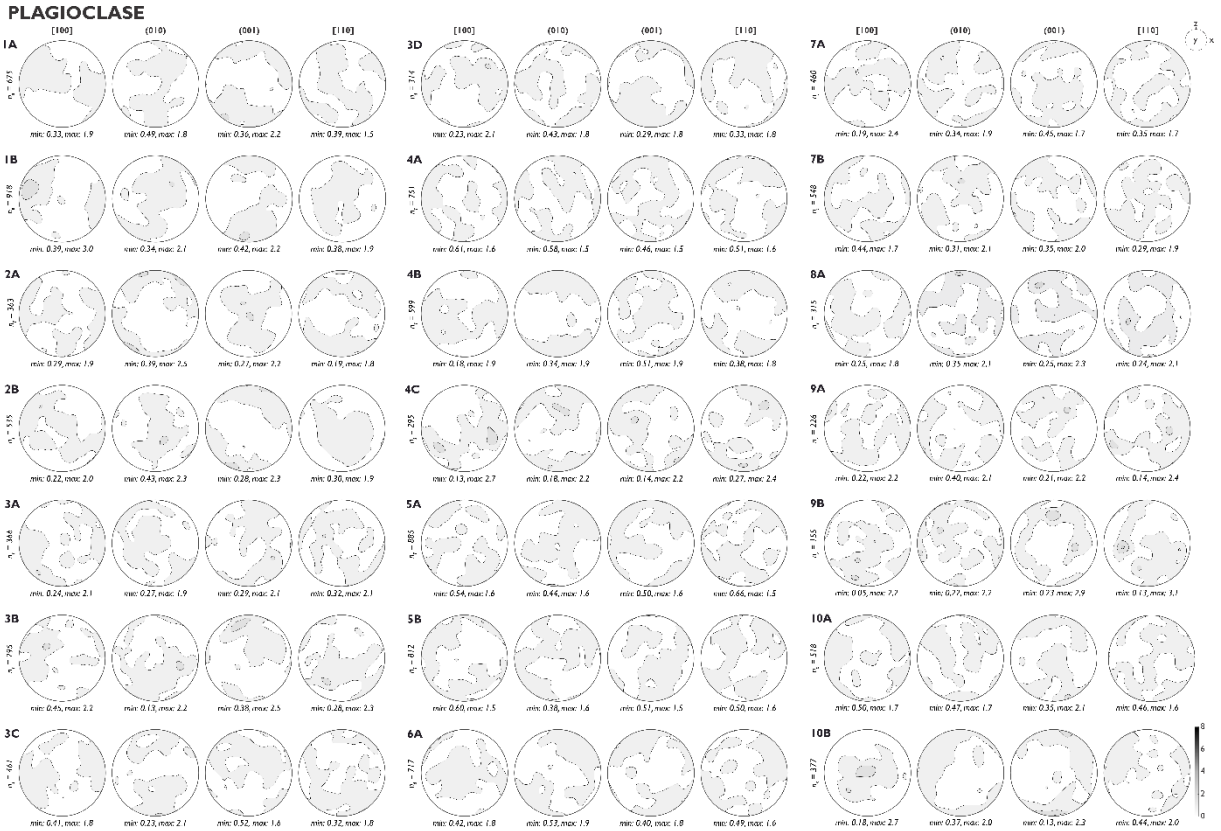

Figure S4: Point per grain, equal area, lower hemisphere plagioclase CPO pole figures.

973